

# Boronic-Acid-Derived Covalent Organic Frameworks: From Synthesis to Applications

Laura Frey,<sup>+a</sup> Jenni J. Jarju,<sup>+b</sup> Laura M. Salonen,<sup>\*b</sup> Dana D. Medina<sup>\*a</sup>

<sup>a</sup> Department of Chemistry, Ludwig-Maximilians-Universität (LMU) & Center for NanoScience (CeNS), Butenandtstr. 11, 81377 Munich, Germany. E-mail: dana.medina@cup.lmu.de

<sup>b</sup> International Iberian Nanotechnology Laboratory (INL), Av. Mestre José Veiga, 4715-330 Braga, Portugal. E-mail: laura.salonen@inl.int

<sup>+</sup> These authors contributed equally.

## Abstract

Modular, well-defined, and robust hierarchical functional materials are targets of numerous synthesis endeavors. Covalent organic frameworks (COFs) are crystalline and porous materials with a vast chemical and structural diversity, and they are synthesized in a bottom-up approach from molecular building blocks by condensation polymerization reactions to form layered or spatial complex structures. Boronic-acid-containing building blocks were the first to be employed as monomers in the synthesis of COFs, setting the foundations for an exceedingly growing, exciting field of research. Here, an overview is provided on boronic-acid-derived COFs, including synthesis, building block design and mechanism of COF formation, structures and properties, processing and implementation in functional devices, as well as examples of application for which these materials have been studied.

## 1. Introduction

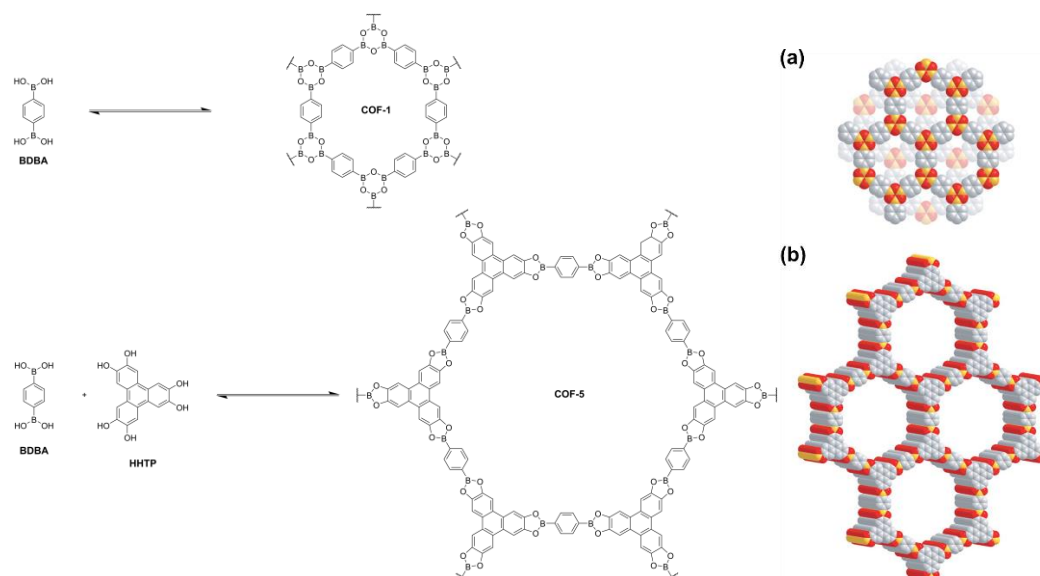
Boronic acids,  $\text{RB}(\text{OH})_2$ , have central roles in synthetic, analytical, and bioorganic chemistry, and they are common precursors in organic chemistry, widely used for catalytic cross-coupling reactions to give saturated carbon-carbon bonds. Therefore, these compounds are broadly commercially available and various synthetic methods have been developed to gain access to them. Boronic acids react through a reversible condensation reaction both with diols to give boronate esters as well as self-condense to yield boroxines. Due to the reversibility of these reactions, the use of boronic acid compounds has been demonstrated for the formation of macromolecular structures, such as macrocycles, molecular cages, and extended frameworks. Both boronate esters and boroxines are planar, thus allowing for predictable connectivity in macromolecule design. The reversible bond formation enables 'proof-reading' and 'error-checking' of the forming structure in a thermodynamically controlled process, thus providing highly structurally defined products.

The two key features of linkage reversibility and planarity have enabled the preparation of boronic-acid-derived highly defined two-dimensional (2D) and three-dimensional (3D) frameworks, the so-called covalent organic frameworks (COFs). COFs are crystalline, light-weight porous materials featuring well-defined pore shape and aperture. The principle of construction of 2D COFs includes

the judicious selection of typically aromatic building blocks with a defined geometry and connecting functional groups, which eventually direct the addition of building blocks in-plane. Upon condensation polymerization, 2D sheets are formed, continuously extending the number aromatic units at the backbone. These extended molecular sheets form aggregates, guided by  $\pi$ - $\pi$  interactions, resulting in a crystalline layered 2D structure and well-defined porous channels, aligned along the stacking direction.

In contrast to layered COFs, where planar molecular monomers are employed, 3D COFs are constructed by employing spatial building blocks, where the connecting vertices are pointing out of plane, thus forming extended 3D networks with different topologies and degree of network interpenetration. In a pioneering work in 2005, Yaghi and co-workers reported the synthesis of 2D COFs<sup>1</sup> through the self-condensation reaction of linear 1,4-benzenediboronic acid (BDDBA) to form boroxines as well as co-condensation of boronic acid compounds with planar catechols to give boronate ester COFs (Fig. 1). In a following work, the same group synthesized extended 3D frameworks employing spatial precursors such as boronic-acid-functionalized tetraphenylmethane. These reports laid the foundations for the discovery of numerous crystalline porous frameworks with vast chemical and physical properties and structural diversity that are known to date.

In this review, we aim to give an overview of boronic-acid-derived COF materials. First, we will focus on the installation of boronic acid moieties to form COF building blocks with the desired functionality and symmetry. Afterwards, the synthesis of boronic-acid-derived frameworks will be discussed with an emphasis on the mechanism of formation and their properties. In addition, different synthesis approaches for the formation of COFs as well as post-synthetic modification methods will be described. Then, the processing of boronic-acid-derived COF powders and thin films will be discussed and the review will conclude with examples of the utilization of these materials for a variety of applications. As an aid to the readers, abbreviations for the most commonly appearing building blocks in this review are presented in Table 1.



**Fig. 1.** A synthesis scheme and structures of (a) COF-1 and (b) COF-5.<sup>1</sup> Reprinted with permission from AAAS.

**Table 1.** Abbreviations for frequently appearing building blocks.

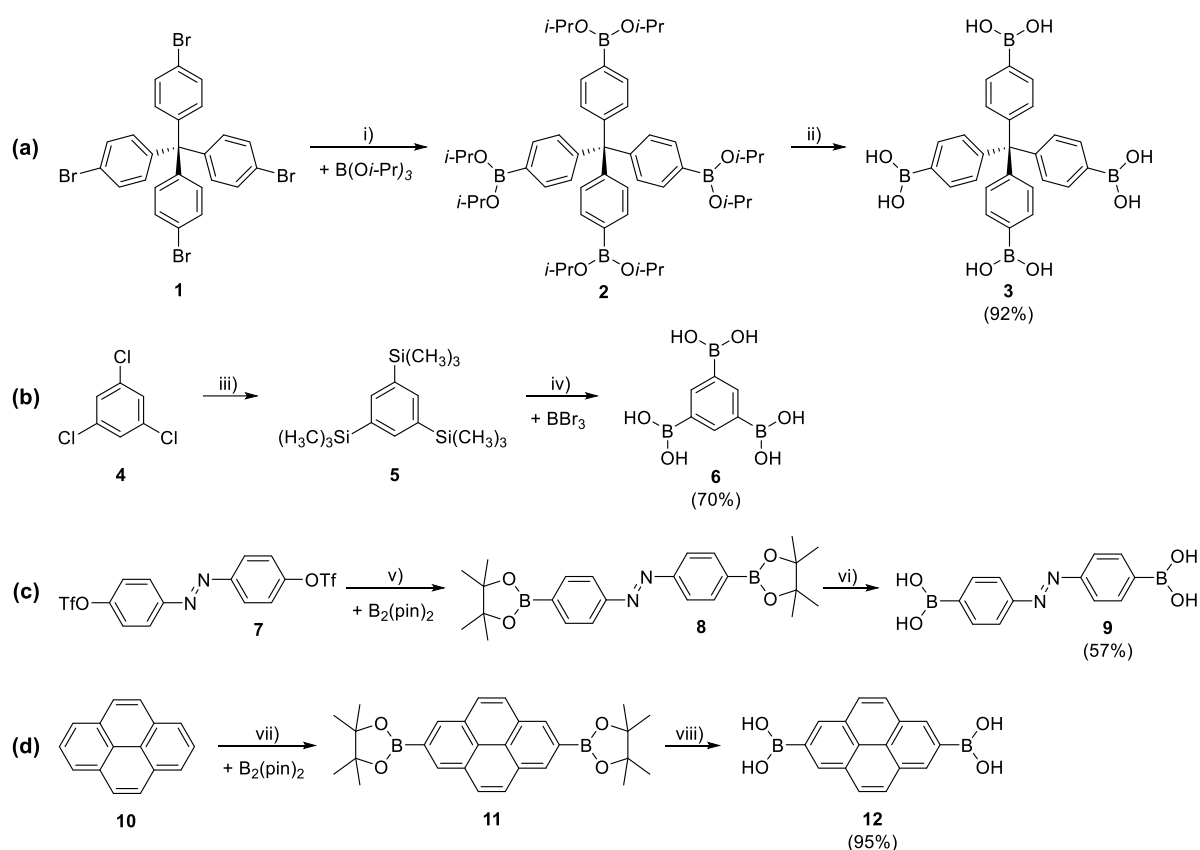
<b>AEM</b>	arylene–ethynylene	<b>NDIDA</b>	naphthalene tetracarboxylic acid diimide
<b>BDBA</b>	1,4-dibenzenediboronic acid	<b>PCBM</b>	[6,6]-phenyl-C <sub>61</sub> -butyric acid methyl ester
<b>BDT</b>	benzo[1,2- <i>b</i> :4,5- <i>b'</i> ]dithiophene	<b>Pc</b>	phthalocyanine
<b>BPDA</b>	4,4'-biphenyldiboronic acid	<b>PDBA</b>	pyrene-2,7-diboronic acid
<b>BPA</b>	borophosphonic acid	<b>PPTODB</b>	4,5,9,10-tetraone-pyrene-2,7-diboronic acid
<b>BTDADA</b>	1,4-benzothiadiazole diboronic acid	<b>PyrDIDA</b>	pyromellitic tetracarboxylic acid diimide
<b>CTC</b>	cyclotricatechylene	<b>TBPM</b>	tetra(4-dihydroxyborylphenyl)methane
<b>DBA</b>	dehydrobenzoannulene	<b>TBPS</b>	tetra(4-dihydroxyborylphenyl)silane
<b>H4TDB</b>	2,5-thiophene diboronic acid	<b>TCAT</b>	4- <i>tert</i> -butylcatechol
<b>HHTP</b>	2,3,6,7,10,11-hexahydroxytriphenylene	<b>THB</b>	tetrahydroxybenzene
<b>MPc</b>	metallophthalocyanine		

## 2. Synthesis and Structure

### 2.1. Installation of the Boronic Acid Functional Group

Boronic acids are trivalent boron-containing organic compounds with one alkyl- or aryl- substituent and two hydroxyl groups. The neutral,  $sp^2$ -hybridized boron center has an empty  $p$ -orbital, which confers Lewis acidity.<sup>2,3</sup> Boronic acids are key building blocks for Suzuki–Miyaura cross-coupling reactions,<sup>4</sup> they can function as selective anion sensors,<sup>5</sup> and form the basis of a myriad of saccharide receptors.<sup>6</sup> Their dynamically reversible condensation reactions, which yield boroxines and boronate esters (see section 2.2), enable the synthesis of complex molecular and supramolecular compounds and materials, such as macrocycles,<sup>7</sup> capsules,<sup>8</sup> polymers,<sup>9</sup> cages, and COFs.<sup>10,11</sup> The increasing importance of boronic acids as synthetic building blocks has led to the development of new mild and efficient synthesis methods to provide a wide range of these compounds with desired functionalities.

In the context of COFs, boronate ester and acid moieties have been incorporated into robust and well-defined building blocks, facilitating COF formation. One of the first, probably the most common, and least expensive methods for the synthesis of arylboronic acids involves the treatment of aryl halides with Grignard or organolithium reagents to produce arylmetal intermediates,<sup>2</sup> followed by a reaction with trialkylborate  $B(OR)_3$  and subsequent hydrolysis of the boronic ester to yield the arylboronic acid (Scheme 1a). Using this method, tetrakis(4-bromophenyl)methane (**1**) was borylated with triisopropyl borate,  $B(OiPr)_3$ , to produce compound **2**, the hydrolysis of which yielded tetraboronic acid **3**.<sup>11</sup> This compound has served as a building block for the synthesis of 3D boroxine COF-102 (section 2.4).<sup>12</sup> Although this synthesis approach is effective for simple systems with small number to no functional groups, finding optimal conditions for high yields can be difficult due to the formation of by-products such as boronic acids and boranes.<sup>2</sup> In addition, the high reactivity of the organometallic intermediates requires inert anhydrous conditions at cryogenic temperatures.



**Scheme 1.** Synthesis of boronic acids **3**, **6**, **9**, and **12**. Reaction conditions: i) *n*-butyllithium in hexane, dry THF; then, triisopropyl borate, dry THF;<sup>11</sup> ii) 1 M HCl; iii) Mg, Me<sub>3</sub>SiCl, dry THF; then H<sub>2</sub>O;<sup>13</sup> iv) BBr<sub>3</sub>, hexane; then, H<sub>2</sub>O; v) KOAc, dppf, 1,4-dioxane, PdCl<sub>2</sub>(dppf)·CH<sub>2</sub>Cl<sub>2</sub>;<sup>14</sup> vi) NaIO<sub>4</sub>, 1 M HCl, THF/H<sub>2</sub>O; vii) [{Ir(μ-OMe)cod}<sub>2</sub>], 4,4'-di-*tert*-butyl-2,2'-bipyridine, dry THF;<sup>15</sup> viii) NaIO<sub>4</sub>, 1 M HCl, THF/H<sub>2</sub>O. dppf: 1,1'-bis(diphenylphosphino)ferrocene; pin: pinacolato; cod: 1,5-cyclooctadiene.

Another common method for preparing relatively simple arylboronic acid derivatives involves the transmetalation of aryl stannanes or silanes<sup>2</sup> with boron tribromide, BBr<sub>3</sub>, yielding arylboron dibromide as intermediate,<sup>10</sup> which can be then converted to arylboronic acid via aqueous acidic workup. Some boronic acids have also been prepared starting from trimethylsilyl derivatives (Scheme 1b). For example, silylation of 1,3,5-trichlorobenzene (**4**) produced compound **5**, which was then borylated with BBr<sub>3</sub> and subsequently hydrolyzed to yield triboronic acid **6**. This compound has been employed together with 2,3,6,7-tetrahydroxyanthracene to give access to a photoresponsive boronate ester COF (section 2.4).<sup>13</sup>

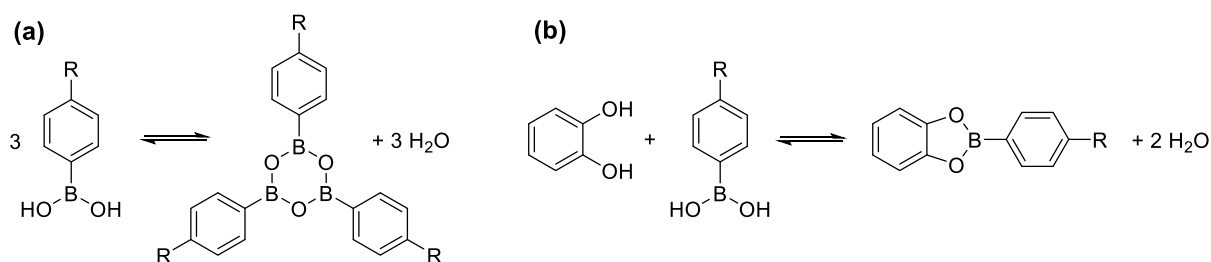
Palladium-catalyzed coupling of an aryl halide or triflate with B<sub>2</sub>(OR)<sub>2</sub> or HB(OR)<sub>2</sub>, such as bis(pinacolato)diboron (B<sub>2</sub>(pin)<sub>2</sub>) or pinacolborane, is an efficient method to provide boronic ester derivatives (Scheme 1c). Hydrolysis of the pinacol ester to the boronic acid proceeds using NaIO<sub>4</sub> under acidic conditions.<sup>2</sup> The method is compatible with a wide variety of haloarene substrates and tolerates the presence of reactive chemical groups such as ketones, esters, nitriles, benzophenones, and benzaldehydes. The reaction is typically completed in less than 24 h. Using this approach, triflate **7** was borylated with B<sub>2</sub>(pin)<sub>2</sub> to yield boronic ester **8**, which was hydrolyzed to azobenzene diboronic acid **9** that, together with 2,3,6,7,10,11-hexahydroxytriphenylene (HHTP, Fig. 1), was used in the synthesis of boronate ester Azo-COF.<sup>14</sup>

A convenient way to prepare boronic acid derivatives is through direct borylation via a transition-metal-catalyzed C–H activation<sup>2</sup> in the presence of a boron donor. This borylation method was first

demonstrated on alkanes using photochemical conditions.<sup>16</sup> For arene substrates, several research groups, including those of Marder,<sup>17</sup> Hartwig,<sup>18,19</sup> and Smith,<sup>20</sup> have reported several efficient procedures using iridium and rhodium catalysts. The main challenge in this method is the regioselectivity of the aromatic C–H activation with mono- and polysubstituted arenes. Marder and co-workers<sup>15</sup> utilized the selectivity of the Ir-catalyzed aromatic borylation of pyrene (**10**) to produce pyrene-2,7-bis(boronate) (**11**) in 97% yield, providing direct borylation of positions that are otherwise difficult to derivatize (Scheme 1d). Perylene-2,5,8,11-tetra(boronate) ester was prepared through a similar procedure in 83% yield. The selectivity is likely obtained owing to the sterics of the bulky Ir-containing intermediate, which is proposed to be the key intermediate performing the rate-determining C–H activation step. Subsequently, compound **11** was hydrolyzed to boronic acid **12**. This compound together with HHTP has been employed in the synthesis of luminescent and semiconductive boronate ester-linked TP-COF (section 2.4).<sup>21</sup> In addition, compound **11** can be further converted into 2,7-bis(R)-pyrenes, where R = BF<sub>3</sub>K, Br, OH or OTf.<sup>22</sup>

## 2.2. Formation of Boroxine and Boronate Ester Compounds

The self-condensation of boronic acids yields planar six-membered boroxine anhydride (B<sub>3</sub>O<sub>3</sub>) rings (Scheme 2a), whereas the condensation of boronic acids with 1,2-diols results in planar five-membered boronic ester (BO<sub>2</sub>C<sub>2</sub>) rings (Scheme 2b).<sup>23</sup> Both boroxine and boronic ester formation are thermodynamically reversible despite the formation of a strong B–O covalent bond, accompanied by the entropically favorable release of water molecules as byproduct, and the bond dissociation energy being 124 kcal mol<sup>−1</sup> for the B–O bond in boronic esters.<sup>24</sup> According to Le Chatelier's principle, the thermodynamic equilibrium of the reactions can be pushed towards products, *e.g.*, by azeotropic removal of water, employing dehydrating agents, and product precipitation. The formation of boroxine anhydrides and boronate esters are fast reactions, with reaction rates of 10<sup>2</sup>–10<sup>3</sup> M<sup>−1</sup> s<sup>−1</sup> for boronate ester formation,<sup>2</sup> which are influenced by the conditions under which the reaction takes place, including the type of solvent and functional groups present on the reactants.

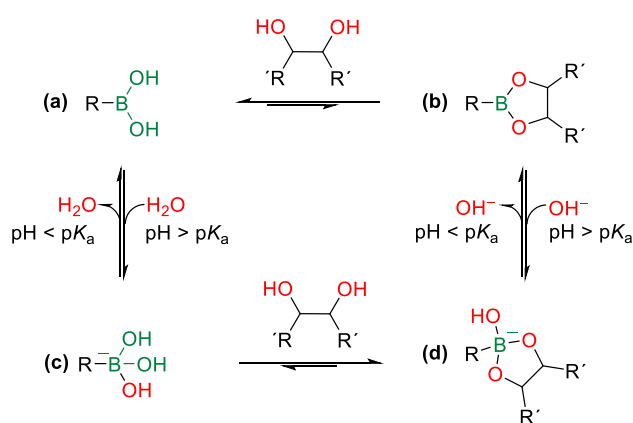


**Scheme 2.** Formation of (a) boroxine and (b) boronate ester compounds.

In nonpolar solvents, many boronic acid derivatives easily self-condense to produce the corresponding less polar boroxines.<sup>23</sup> Boron compounds functionalized with electron-donating groups have been reported<sup>24</sup> to promote boroxine formation by decreasing the electrophilicity of the boron. The resulting ring is therefore less prone to hydrolysis, whereas electron-withdrawing groups have a destabilizing effect on the formed ring.<sup>25</sup> Compounds with nitrogen Lewis base donors, such as pyridine, facilitate the

self-condensation of boronic acids by forming a boroxine–N-donor adduct, the formation of which is thermodynamically more favorable than that of uncoordinated boroxine.<sup>2,23</sup>

The water stability of boronate esters is significantly influenced by the structure of the diol precursor, with cyclic and hindered *cis*-1,2-diols, giving typically access to more stable products.<sup>26</sup> The lower polarity of boronate esters compared to the corresponding boronic acids can be used to shift the equilibrium towards ester formation in nonpolar solvents.<sup>23</sup> In aqueous medium, the ionic equilibrium between boronic acid (**a**) and boronate anion (**c**) is shown on the left of Scheme 3. Acidic conditions favor the formation of electron-accepting boronic acid, while under basic conditions the electron-donating boronate anion dominates.<sup>27</sup> Since **a** and **c** have different electronic properties, the reactions involving boronic acids are dependent on the equilibrium between the boronic acid and the boronate anion. The reaction of boronic acids with diols forms both boronate esters (**b**) and boronate ester anions (**d**), which exist in ionic equilibrium. The formation of the tetrahedral boronate anion **c** has been assumed to favor complexation with diols at higher pH values, yielding boronate esters, while under acidic conditions boronate esters tend to hydrolyze.<sup>26</sup> The reactivity and formation constant of boronic acids (**a**) increase with their increasing acidity, whereas the opposite is found for the conjugate base (**c**): the higher basicity of **c** leads to higher reactivity with diol forming boronate ester anion **d**.<sup>27</sup> Additional stability to the boronate ester is provided by *o*-substitution of the phenylboronic acid. The  $pK_a$  of phenylboronic acid is 8.8, which is slightly more acidic than boric acid ( $pK_a = 9.2$ ) and less acidic than 3,5-dichlorophenylboronic acid ( $pK_a = 7.4$ ) or 4-nitrophenylboronic acid ( $pK_a = 7.1$ ).<sup>2</sup> Boronic acids become more acidic upon diol binding, the  $pK_a$  values of the boronate esters being 2–4 units lower compared to the  $pK_a$  of the corresponding boronic acid.<sup>28</sup>



**Scheme 3.** The pH-dependent formation equilibrium of a boronic ester in aqueous solution.

### 2.3. COF Synthesis and Mechanism of Formation

Although many building blocks and synthesis routes have been developed to obtain crystalline COFs, finding suitable reaction conditions under which a COF forms is still not trivial.<sup>29</sup> Regulating the thermodynamic equilibrium during covalent bond formation is a key to obtain highly crystalline and porous COFs, where temperature, pressure, and solvents all play a pivotal role.

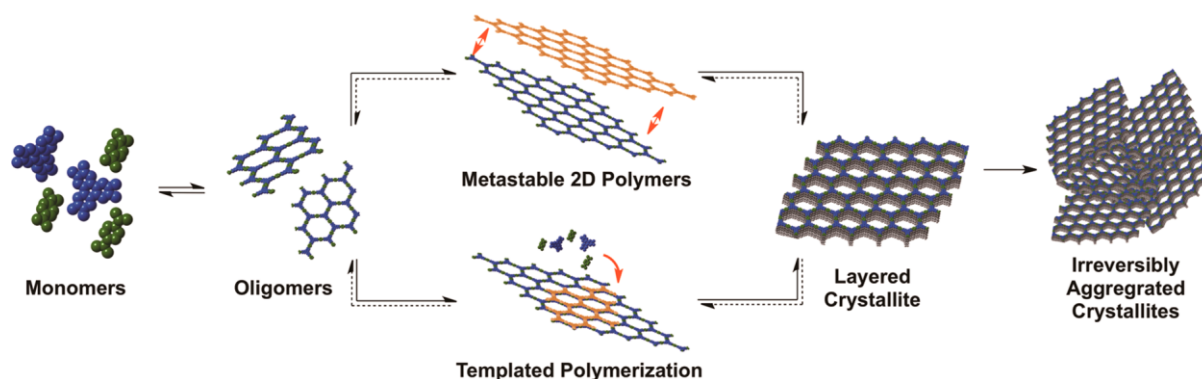
Solvothermal synthesis is the most typical preparation method of boronic-acid-derived COF materials, and it often requires several days within a sealed vessel at a constant elevated temperature, ranging

from 80–120 °C.<sup>29</sup> Solvent combinations and ratios chosen for the COF synthesis are important factors, as they affect the polarity of the medium and thereby the solubility of the building blocks, the reaction rate, crystal nucleation, crystal growth rate, and reversibility of the reaction, which in turn allows for self-healing and ‘error-correction’ in the process. During an optimal COF synthesis, should a linkage form in an undesired direction, reversible bond formation grants access to its repair, thus ultimately leading to a crystalline, stable product.<sup>30</sup> Mixtures of apolar and polar solvents, such as mesitylene/dioxane or *o*-dichlorobenzene/dimethylacetamide (DMAc), are commonly employed in the synthesis of boronate-ester and boroxine-linked COFs. A suitable concentration of the building blocks in the solvent system is essential for the reaction to proceed under thermodynamic control.

Although solvothermal synthesis is widely used and leads to highly crystalline and porous COF materials, the challenges include the relatively long reaction times and scale-up of COF synthesis.<sup>31</sup> An approach to overcome these challenges was reported by Cooper and co-workers,<sup>32</sup> who synthesized 2D COF-5 (Fig. 1) and 3D COF-102 (section 2.4) using microwave heating in only 20 min. The reaction proceeded over 200 times faster for both COFs as compared to the solvothermal method and resulted in nearly double Brunauer–Emmett–Teller (BET) surface area for COF-5. The possibility of conducting the reaction in an open vessel facilitates the optimization of the conditions and paves the way for industrial production. In another approach, COFs were produced through sonochemical synthesis.<sup>33</sup> The use of ultrasound irradiation forms micrometer-sized bubbles in the solvent, which grow and collapse in a cavitation process. This leads to high local temperatures and pressures in the solution, and thus accelerates chemical reactions. This method was used for the preparation of COF-1 and COF-5, and materials with BET surface areas of over 2000 m<sup>2</sup> g<sup>-1</sup> were obtained in a short reaction time of 0.5–2 h. The scalability of this technique was demonstrated up to 0.5 L batch size, showing potential for the synthesis of highly porous products on a large scale with a space–time yield of COF-5 being 45 kg m<sup>-3</sup> day<sup>-1</sup>. The sonochemical method was also used to deposit COF-5 on carbon nanotubes (CNTs) and graphene.<sup>31</sup>

Despite intense research in COF materials, the nucleation and growth processes of the frameworks remain poorly understood. In most COF syntheses, the monomers are only partially soluble under the reaction conditions and the product and intermediates precipitate from the reaction mixture. Therefore, the reaction solution is heterogeneous at all times, which excludes the use of most *in situ* spectroscopic characterization techniques that would give important information of COF polymerization and crystallization processes.<sup>34</sup> To shed light on the COF formation processes, several mechanistic studies on boronate ester 2D COFs have been carried out by Dichtel and co-workers.<sup>34–37</sup> Here, COF-5 was synthesized starting from clear, fully-soluble monomer solutions, which provided COF material with high crystallinity and surface area, and allowed for the measurement of the rate of formation of COF-5 and determination of its formation under varied reaction conditions.<sup>34</sup> Homogeneous solutions were obtained by the addition of a small amount of MeOH as modulator to 4:1 dioxane/mesitylene mixture, from which COF-5 started to precipitate upon heating to 90 °C, enabling the quantification of its formation rate from optical turbidity measurements. The precipitation of crystalline COF-5 was found to begin already after a two min induction period and proceed at a constant rate for several minutes, after which the COF precipitation started to slow down. The growth rate was further studied under various homogeneous

reaction conditions to provide information on the bond-forming and crystallization processes, controlling the temperature, concentration, as well as the concentration of the modulator and the co-solvent.<sup>34</sup> The obtained insights led to a model for COF-5 formation (Fig. 2), which suggests that the early stages of boronic-acid-derived COF synthesis involve monomer condensation into soluble oligomers, followed by a nucleation step yielding COF crystallites, which further grow by bond-forming and stacking processes. The small crystallites aggregate and precipitate as polycrystalline powders with high surface areas, confirming the hypothesized COF precipitation process. The precipitation happens in minutes when reaction-rate-inhibiting additives, such as H<sub>2</sub>O, an excess of MeOH, or monofunctional 4-*tert*-butylcatechol (TCAT), are not present in the reaction mixture. The TCAT modulator serves as a steric capping agent of the boronic acid precursor, lengthening the induction period and inhibiting precipitation, thus suppressing further COF nucleation without preventing seeded growth. Furthermore, dynamic boronate ester exchange occurs among soluble monomers and oligomers and probably at the edges of the growing crystals prior to precipitation. The study suggested that 2D and 3D boronate ester and boroxine COF syntheses proceed through reversible bond-formation processes, which are capped by at least one irreversible step associated with the precipitation of a nanocrystalline product.



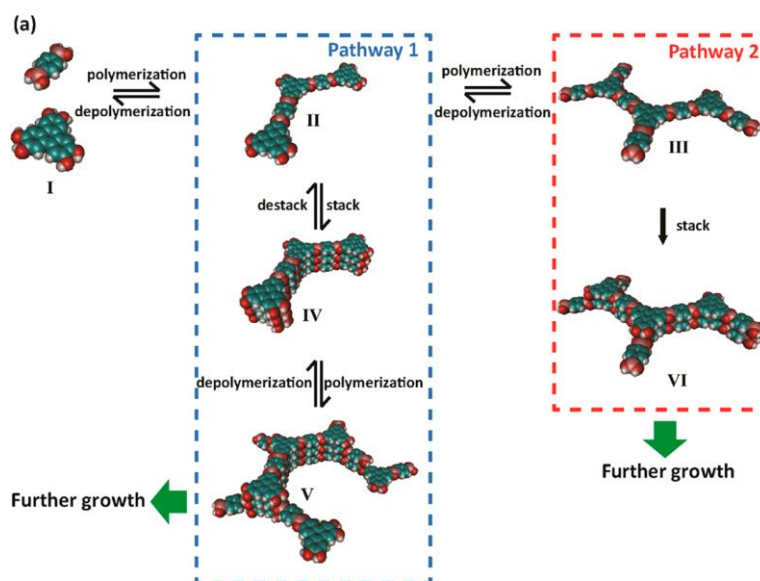
**Fig. 2.** Proposed models of boronate ester COF-5 growth. Reprinted with permission.<sup>34</sup> Copyright (2014) American Chemical Society.

The proposed COF formation model was further studied by systematically varying monomer length and aromatic domain size of 2D boronate ester COFs, namely COF-5 (Fig.1), COF-10 (Table 2), HHTP-DPB COF (Table 2), and TP-COF (Table 2).<sup>35</sup> Turbidity measurements indicated that formation of all four COFs begins with a fully soluble monomer induction period that is followed by a rapid increase in turbidity associated with COF precipitation. The COF formation rates depend on both pore size and the interlayer attractive forces: the growth rate was found to increase with enhanced van der Waals surface of the linkers, whereas larger pore size and the corresponding higher percentage of empty space per unit cell, decreasing the interlayer attraction, led to decreased rates. To determine the overall activation energies for the COF formation reactions, the syntheses were carried out at different temperatures. The cause of activation energy differences was further studied by examining the formation of molecular boronate esters in condensation reaction of 2,7-pyrenebisboronic acid monomers, used in the synthesis of TP-COF, and BDPA of COF-5 with TCAT under similar conditions. The activation energies for boronate formation are similar for both linkers, ca. 7 kcal mol<sup>-1</sup>, which is significantly lower than the COF formation energies, indicating that the initial boronate ester formation is not the rate-determining step for these COFs. Furthermore, the water stability of the COFs was examined and the results are consistent with

the relative growth rates, showing that COFs with smaller pore size and greater intermolecular interactions also demonstrated greater water stability. These results indicate that interlayer stacking of the 2D polymers is the rate-determining step, and that COF formation occurs through nucleation–elongation type mechanism, in which a 2D polymer templates the growth of a subsequent COF layer.

Experimental and theoretical studies were combined to estimate the rate parameters associated with the nucleation and growth of COF-5.<sup>36</sup> A kinetic Monte Carlo (KMC) model was used to describe the formation of the COF from its monomers in solution, deriving the key rate parameters from experimental measurements when possible. To understand the structure of the nuclei and the nucleation process, KMC simulations were carried out monitoring all generated intermediate structures once they had reached a certain number of monomer units ( $N$ ). The model suggested that small oligomers, for example with  $N = 15$ , rarely grow into COF-5 crystals, with the majority decomposing back to smaller units. In contrast, larger oligomers with  $N \geq 30$  almost always grow into crystals. The nucleation process includes the formation of stable stacked structures that are able to grow further before they dissociate to oligomers and monomers. The rate of the stacking process is fast with negligible energy barrier, frequently giving rise to multi-layered structures, while COF layer defoliation rate is highly dependent on the size of the oligomers. Larger oligomers have larger lateral sizes, and thus increased stability.

The nucleation process of COF-5 was found to have several stages, resulting in multilayer structures.<sup>36</sup> The first stage is the formation of small oligomers, which influences the length of the induction period. The oligomers formed in the first step, then follow two different nucleation pathways (Fig. 3). In the first pathway, stacking of the small oligomers results in larger structures, from which the majority dissociates back to oligomers, and a smaller population successively grows laterally. The nucleation pathway two includes lateral growth of the small oligomers to form larger ones, which can then stack and produce stable nuclei that can grow further. One pathway does not rule out the other: if the first pathway fails, the oligomers formed in it are able to participate in the second nucleation pathway. After the formation of a nucleus, the growth continues into a COF-5 crystal in a process, where both lateral diameter and height increase linearly with time. The lateral growth occurs *via* bond formation with monomers and small oligomers, while vertical growth, corresponding to the formation of new layers, is dominated by oligomers. Adding water to the reaction mixture gives rise to COF-5 crystals with larger diameters by shifting the equilibrium from large oligomers towards monomers, thereby favoring lateral (pathway 1) over vertical growth (pathway 2). The crystallization of COF-5 is non-classical and similar to crystallization by particle attachment (CPA),<sup>38–40</sup> since oligomers are the key precursors in the nucleation process and dominate vertical growth. On the other hand, as opposed to the CPA mechanism, COF-5 crystallization involves several metastable species like oligomers and stacked structures in the nucleation process, different mechanisms in vertical and lateral growth, and simultaneous presence of the classical monomer-by-monomer addition mechanism that dominates the lateral growth of the COF-5 crystals.



**Fig. 3.** Two observed nucleation pathways for COF-5. Reprinted with permission.<sup>36</sup> Copyright (2017) American Chemical Society.

Further experimental studies of nucleation and growth mechanisms included a quantitative analysis of the nucleation–elongation dynamics of 2D COFs. The rate dependence of COF-5 nucleation and growth was investigated by *in situ* small/medium/wide-angle X-ray synchrotron scattering (SAXS/MAXS/WAXS) measurements, which allow for monitoring of the size and crystallinity of the particles as the reaction proceeds.<sup>37</sup> To examine the nucleation and growth processes independently, such monomer concentrations were selected under which one process is dominating. The results indicated that the nucleation and growth processes have second-order and first-order dependences on the monomer concentration, respectively, meaning there exists a critical monomer concentration ( $C^*$ ) below which nucleation impedes growth is the dominating process. This result is in line with earlier findings that nucleation is suppressed when adding monomers slowly to a colloidal suspension,<sup>41</sup> and because of that, lower monomer concentration yields fewer but larger crystallite domains. In contrast, if the monomer concentration is higher than  $C^*$ , the successive nucleation takes place with the growth process, resulting in a smaller average crystal size.

## 2.4. COF Structures and Properties

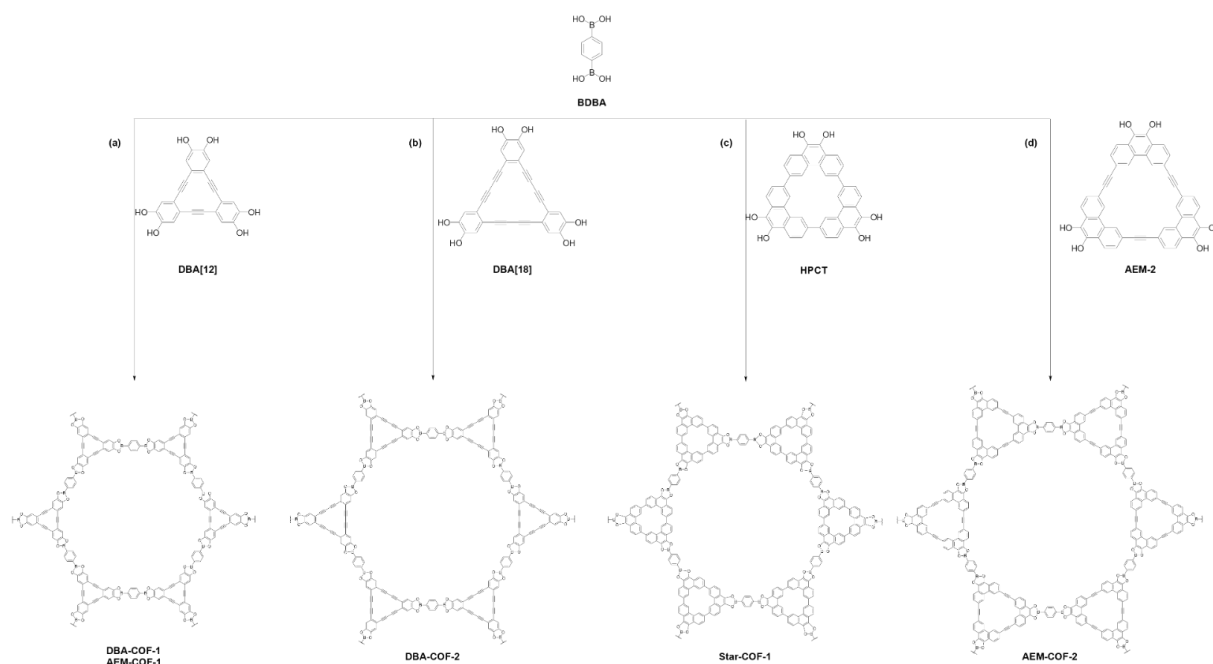
Through the combination of multidentate building blocks, various COF pore systems can be designed using the principles of reticular chemistry, resulting in a broad range of pore sizes, topologies, and geometries. This way, hexagonal, quadratic, pseudo-quadratic/rhombic, trigonal, or dual-pore/star-shaped pore systems can be achieved. Additionally, vast opportunities for the pre-design of COF pore-wall surfaces are presented through the selection of functional groups decorating the organic building units. Following the pioneering report<sup>1</sup> of boroxine and boronic ester COF syntheses by Yaghi and co-workers (Fig. 1), a wide variety of different structures have been presented. Two-dimensional boronate ester COFs (Table 2 and Table 3) are by far the most common boronic-acid-derived COFs, although interesting examples have also been reported on boroxine (Table 4) and 3D COFs (Table 5). Selected structures of these COF classes will be presented in the following, and this section is concluded

with examples of double-linkage COFs, which feature an additional linkage type to the boronic ester (Table 6).

The synthesis of one of the first COFs, COF-1, was based on a simple molecular dehydration process of BDBA at 120 °C for 72 h in a mesitylene/dioxane mixture, resulting in a highly crystalline boroxine-linked framework.<sup>1</sup> Comparing the experimental powder X-ray diffraction (XRD) pattern to the one of the simulated model revealed that the 2D organic sheets arrange in a staggered manner (AB), analogous to the packing of graphite sheets, where the vertex of one layer is located at the pore opening of the successive layer (Fig. 1a). This layer arrangement was attributed to the presence of residual mesitylene within the pores and upon removal of the solvent guest molecules, the layers shifted towards an eclipsed AA stacking mode, where the successive layers are fully overlapped. In the case of COF-5 (Fig. 1b), eclipsed AA stacking of the 2D layers was observed, which was attributed to the presence of the conjugated HHTP units, inducing favorable  $\pi$ - $\pi$  interactions between successive layers.

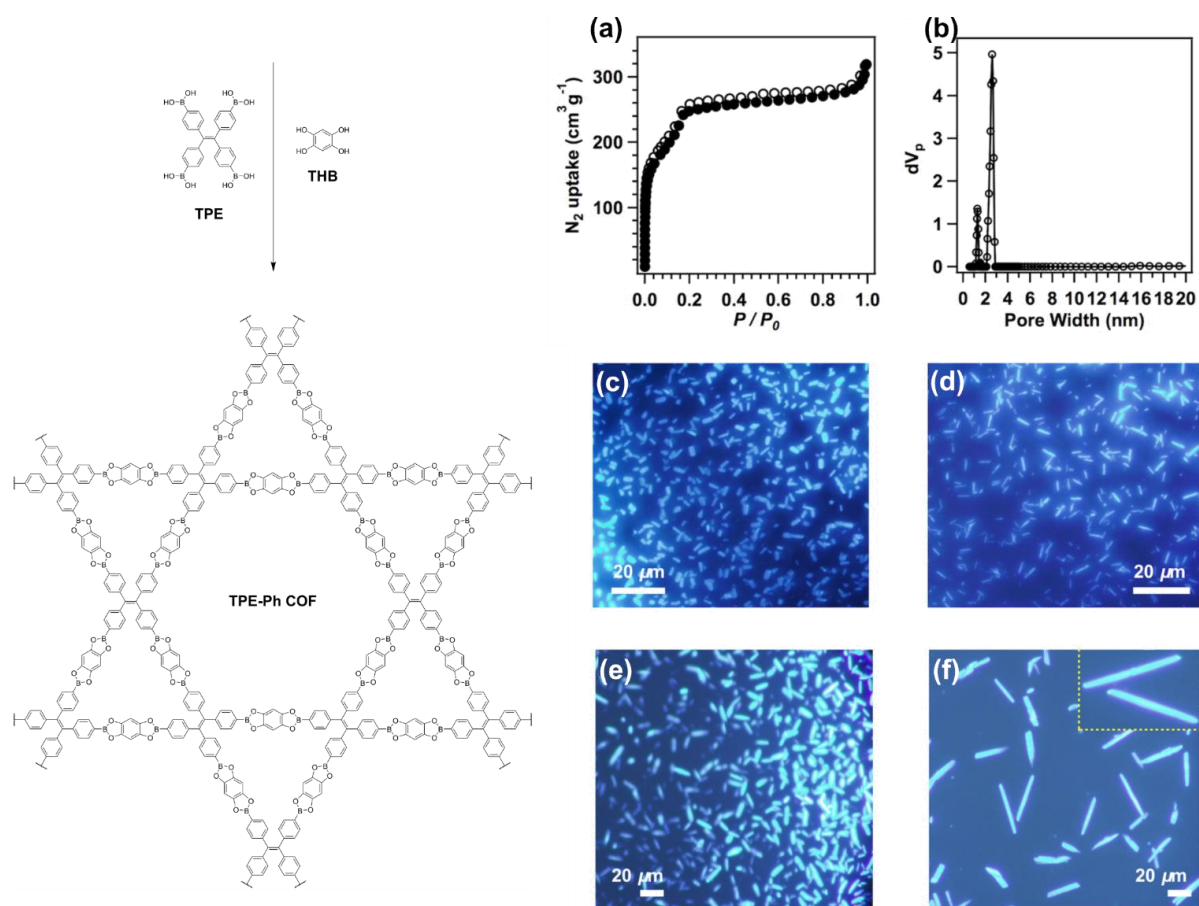
Eclipsed layer arrangement was also found for boroxine-linked PPy-COF (Table 4), formed by the self-condensation of pyrene-2,7-diboronic acid (**12**) (PDBA, Scheme 1d) units, which was attributed to the extended  $\pi$ -system of pyrene.<sup>42</sup> This COF exhibited interesting photophysical properties by visible light absorption: upon excitation at 414 nm photon, emission at  $\lambda = 484$  nm was observed, triggering photocurrent generation, thus representing the first example of a photoconductive COF. Luminescent and semiconducting properties were also found when the same pyrene building block was combined with HHTP, resulting in the belt-shaped TP-COF,<sup>20</sup> which, similarly to PPy-COF, was found to be highly luminescent and electrically conductive.

Dual-pore COFs with alternating triangular and hexagonal pores based on the combination of  $C_3$ -symmetric  $\pi$ -conjugated dehydrobenzoannulenes (DBAs) with BDBA (Scheme 4a,b) were reported to feature luminescent properties ( $\lambda_{\text{max}} = 530$  nm, with  $\lambda_{\text{exc}} = 365$  nm) with an absorption range of 310–380 nm.<sup>43</sup> DBAs are planar macrocycles that form strong metal complexes with Li, Ca, and low-oxidation-state transition metals by donating 2–4 electrons per alkyne as required by the electronic demands of the metals. The small DBA[12] macrocycle has also been converted to a 3D COF with tetra(4-dihydroxyborylphenyl) methane (TBPM).<sup>44</sup> COFs with luminescent properties have been obtained from DBA[12] and DBA[18] in combination with PDBA, yielding Py-DBA-COF 1 and Py-DBA-COF 2, respectively.<sup>45</sup> In addition, a mixed-linker approach using both DBA[12] and DBA[18] gave access to Py-MV-DBA-COF. All three COFs were highly luminescent in the solid state. For DBA-COF 2, a blue-greenish luminescence was observed with  $\lambda_{\text{max}} = 483$  nm upon excitation at 365 nm. In contrast to that, Py-DBA-COF 1 and Py-MV-DBA-COF both revealed red-shifted luminescence at  $\lambda_{\text{max}} = 530$  nm and  $\lambda_{\text{max}} = 528$  nm, respectively, leading to the conclusion that the luminescence of the multicomponent structures is mostly dominated by the DBA[12] units. Other dual-pore COFs have been reported using  $C_3$ -symmetric 9,10-hydroxyphenanthrene trimeric macrocycle (HPCT, Scheme 4c),<sup>46</sup> the condensation of which with BDBA, PDBA, and biphenyldiboronic acid led to a series of COFs with star-shaped topology. This macrocycle-to-framework strategy was expanded by using tritopic arylene-ethynylene macrocycles (AEMs, Scheme 4d).<sup>47</sup>



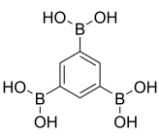
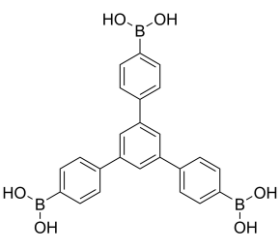
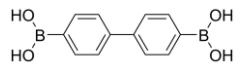

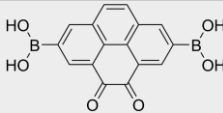
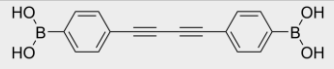
**Scheme 4.** Examples of COFs with a dual-pore structure: (a) DBA-COF-1<sup>43</sup>/AEM-COF-1,<sup>47</sup> (b) DBA-COF-2,<sup>43</sup> (c) Star-COF-1,<sup>46</sup> and (d) AEM-COF-2.<sup>47</sup>

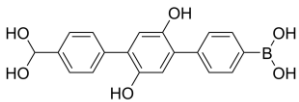
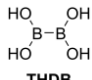
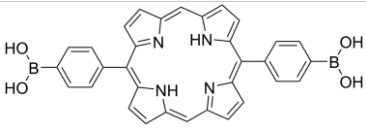
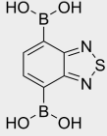
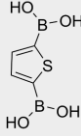
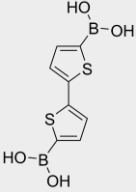
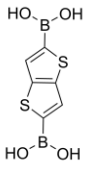
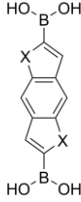
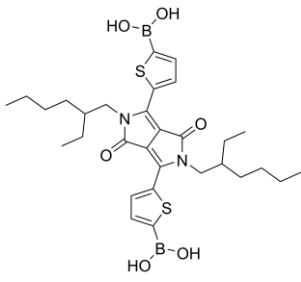
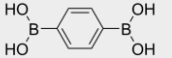
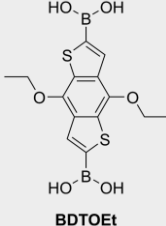
In all of the above-mentioned dual-pore macrocycle COFs, the presence of the micropores could not be confirmed from the N<sub>2</sub> sorption isotherms, indicating low accessibility of the smaller pores. Contrarily, TPE-Ph COF formed from the boronic acid analog of 1,1,2,2-tetraphenylethylene (TPE) with tetrahydroxybenzene (THB) exhibited a dual-pore system with accessible trigonal pores, featuring different pores of 1.3 and 2.6 nm in size (Fig. 4a,b).<sup>48</sup> This COF also exhibited aggregation-induced emission (AIE), meaning that the chromophores become emissive in aggregated state, thus overcoming aggregation-caused quenching (ACQ) that had previously limited the availability of highly emissive COFs, thus granting access to these ordered, porous structures for sensing and imaging applications. The TPE unit provides a specific docking site for successive layers owing to its highly defined locked propeller shape. Thus, rotation-induced excitation-energy dissipation was hindered, resulting in an absolute fluorescence quantum yield as high as 32%. The fluorescence microscopy images of TPE-Ph COF samples prepared at different reaction times show that the synthesis time and thus the crystal shape did not alter the luminescent properties of the material (Fig. 4c–f).



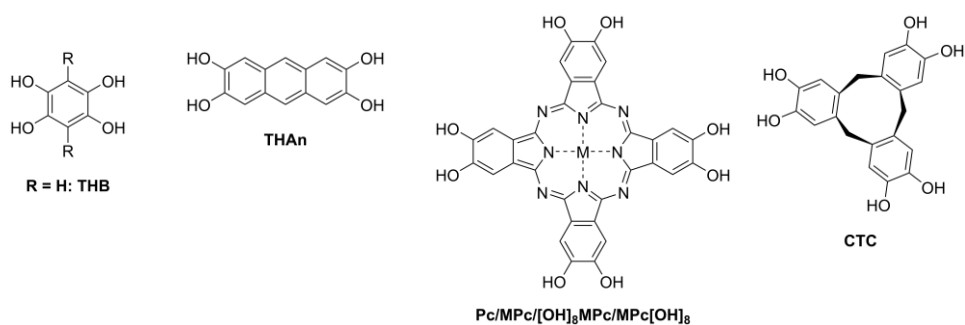
**Fig. 4.** Synthesis of dual-pore TPE-Ph COF, (a)  $N_2$  adsorption and desorption isotherms and (b) pore size distribution profile of TPE-Ph COF and the fluorescence microscopy images of TPE-Ph COF samples prepared at different reaction times of (c) 3 days, (d) 10 days, (e) 20 days, and (f) 30 days. Adapted with permission.<sup>48</sup> Copyright (2016) American Chemical Society.

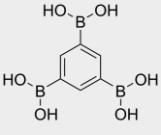
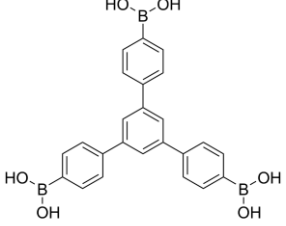
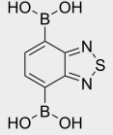
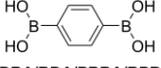
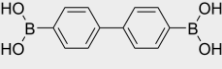

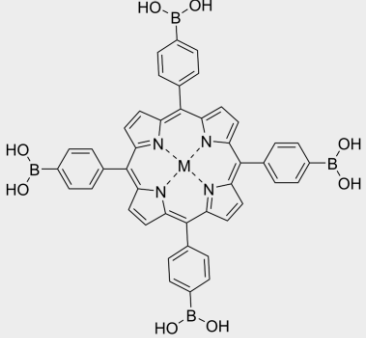
**Table 2.** Examples of HHTP-based 2D boronate ester COFs.

 <p><b>BTBA/TBA</b></p> <p><b>COF-6<sup>49</sup></b></p>	 <p><b>BTPB/BTPA</b></p> <p><b>COF-8<sup>49</sup></b></p>	 <p><b>BPBA/BPDA/DPDA</b></p> <p><b>COF-10<sup>49</sup></b></p>
 <p><b>PDBA/PDA</b></p> <p><b>TP-COF<sup>21</sup></b></p>	 <p><b>Dione-COF<sup>50</sup></b></p>	 <p><b>DPBA/DPBDDA</b></p> <p><b>HHTP-DPB COF<sup>51</sup></b></p>

 <p><b>DHTBA</b></p> <p><b>T-COF-OH<sup>52</sup></b></p>	 <p><b>THDB</b></p> <p><b>HTCOF<sup>53</sup></b></p>	 <p><b>Por</b></p> <p><b>TP-Por COF<sup>54</sup></b></p>
 <p><b>BTDADA</b></p> <p><b>2D D-A sCOF<sup>55</sup></b></p>	 <p><b>H<sub>4</sub>TDB</b></p> <p><b>T-COF-1<sup>56</sup></b></p> <p><b>T-COF-2<sup>56</sup></b></p>	 <p><b>H<sub>4</sub>BTDB</b></p> <p><b>T-COF-3<sup>56</sup></b></p>
 <p><b>H<sub>4</sub>TTDB/TTBA/TTDA</b></p> <p><b>TT-COF<sup>57,58</sup></b></p> <p><b>T-COF-4<sup>56</sup></b></p>	 <p><b>X = S: BDT/BDTBA/H<sub>2</sub>BDS/BDTBA</b>  <b>X = Se: H<sub>2</sub>BDS<sub>Se</sub></b>  <b>X = Te: H<sub>2</sub>BDTe</b></p> <p><b>X = S BDT-COF,<sup>59-62</sup> 1-S<sup>63</sup></b>  <b>X = Se 1-Se<sup>63</sup></b>  <b>X = Te 1-Te<sup>63</sup></b></p>	 <p><b>DPP2</b></p> <p><b>DPP2-HHTP-COF<sup>64</sup></b></p>
 <p><b>BDBA/BDPA/PBBA/BPBA</b></p> <p><b>COF-5<sup>1</sup></b></p>	 <p><b>BDT-OEt</b></p> <p><b>BDT-OEt COF<sup>62</sup></b></p>	

**Table 3.** 2D boronic ester COFs.



 <p><b>BTBA/TBA</b></p>	<p><b>R = H</b> <b>COF-18Å<sup>65</sup></b></p> <p><b>R = CH<sub>3</sub></b> <b>COF-16Å<sup>65</sup></b></p> <p><b>R = CH<sub>2</sub>CH<sub>3</sub></b> <b>COF-14Å<sup>65</sup></b></p> <p><b>R = CH<sub>2</sub>CH<sub>2</sub>CH<sub>3</sub></b> <b>COF-11Å<sup>65</sup></b></p>	<b>Ph-An COF<sup>13</sup></b>		
 <p><b>BTPB/BTPA</b></p>		<b>BTP-COF<sup>66</sup></b>		
 <p><b>BTDA</b></p>			<b>M = Ni</b> <b>2D-NiPc-BTDA COF<sup>67</sup></b>	
 <p><b>BDBA/BDA/PBBA/BPBA</b></p>				<b>CTC-COF<sup>68,69</sup></b>
 <p><b>BPBA/BPDA/DPDA</b></p>				<b>CTC-COF-2<sup>70</sup></b>
 <p><b>PDBA/PDA</b></p>				<b>CTC-COF-3<sup>70</sup></b>
 <p><b>MP</b> <b>(M = H<sub>2</sub>, Zn, Cu)</b></p>	<p><b>H<sub>2</sub>P-COF<sup>71,72</sup></b> <b>ZnP-COF<sup>71</sup></b> <b>CuP-COF<sup>71</sup></b></p>			

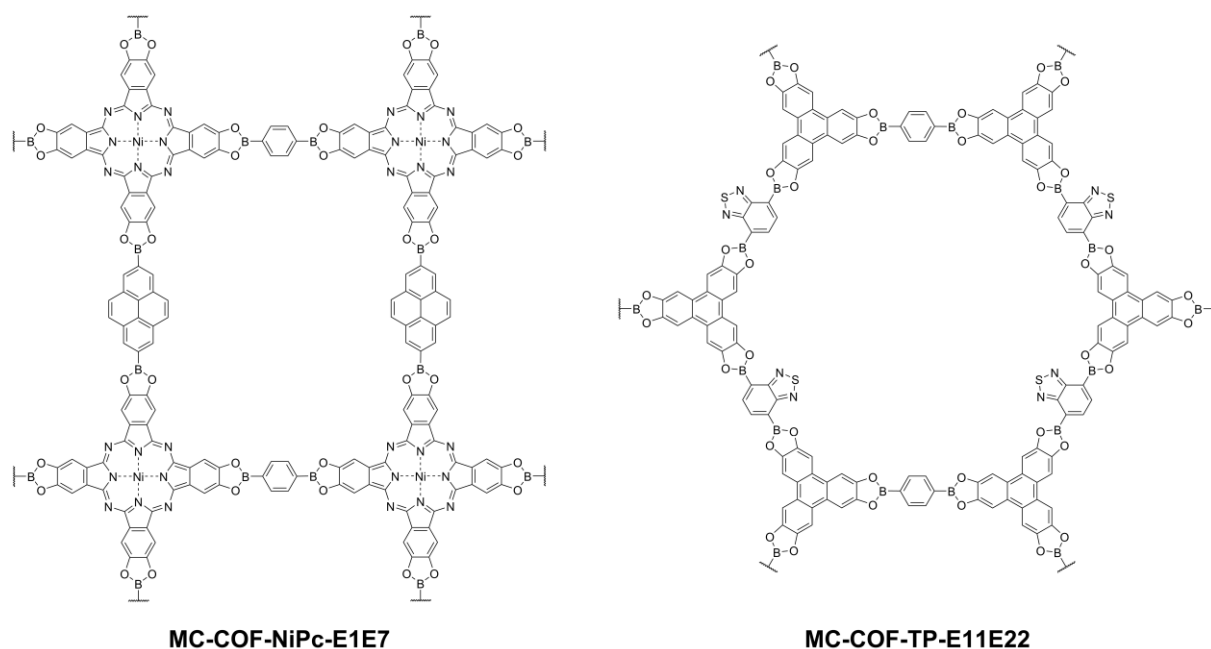
Owing to their stability, planarity and rigidity, free-base and metallophthalocyanines (MPcs) have been widely used across the fields of material science for semiconductors, electrochromic and non-linear optical devices, and catalysis.<sup>73</sup> However, polymeric phthalocyanine materials usually lack either the control of molecular alignment or long-range order, which are crucial when designing functional

materials since device performance can be strongly dependent on the structural order. Thus, incorporation of these molecules into COFs is an attractive way to control their chemical environment. To date, phthalocyanines (Pcs) have been widely used as core building blocks for boronate ester COFs, which, in combination with linear building blocks, lead to tetragonal pore structures.<sup>74</sup> In addition to the typical condensation reaction between boronic acids and diols, a successful preparation of Pc-containing COFs from acetonide-protected octahydroxyphthalocyanine by Lewis-acid catalyzed *in situ* deprotection has been reported.<sup>75</sup>

Pcs feature great electron-donating properties, they readily engage in  $\pi$ - $\pi$  stacking interactions, and their properties can be easily tuned by the choice of the core metal. MPc COFs having different central metal species ( $M = \text{Co}, \text{Cu}, \text{Zn}$ ) have been reported to provide good pathways for charge-carrier transport.<sup>76</sup> Flash-photocatalysis time-resolved microwave conductivity (FP-TRMC) measurements showed that the different central metals led to different charge carrier mobilities, meaning that the charge carrier transport throughout the framework is strongly influenced by the metal species. These metal species are coordinated in the phthalocyanine by four nitrogen atoms leading to a lower electron density of the macrocycles in the following way:  $\text{CuPc-COF} < \text{ZnPc-COF} < \text{CoPc-COF}$ . MPc COFs also give rise to *n*-channel semiconductors featuring broad absorption range, panchromatic photoconductivity, high near infra-red (NIR) sensitivity, as well as high charge carrier mobility.<sup>67</sup> 2D-NiPc-BTDA COF (Table 3) formed from the electron-withdrawing 1,4-benzothiadiazole diboronic acid (BTDA) and a Ni-based Pc gave access to AA-stacked layers, which provided pathways for charge carrier transport and mobilities.<sup>67</sup>

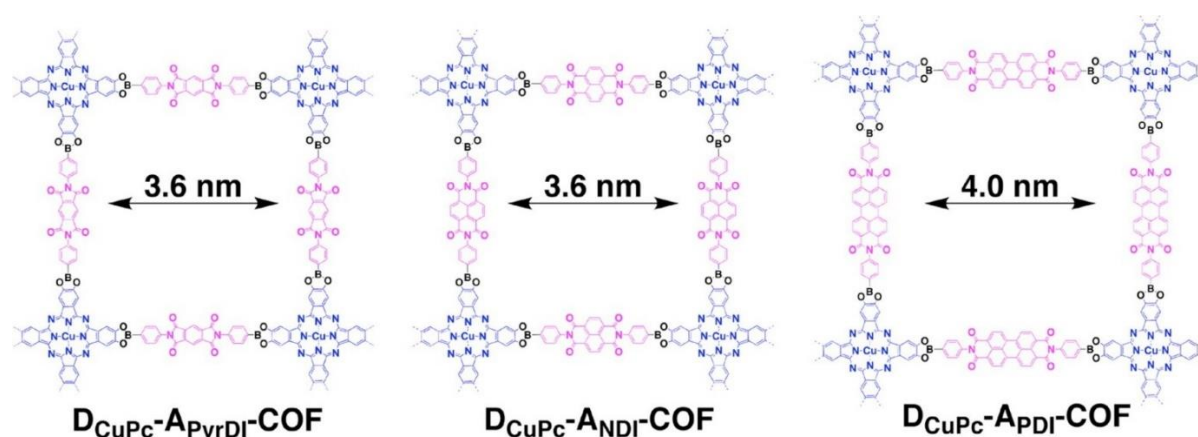
A series of studies have focused on constructing COFs containing both electron donor and acceptor units within their framework to provide highly ordered heterojunctions within the COF lattice. A COF consisting of HHTP donor and benzothiadiazole acceptor units showed large on/off photoconductive response and a high-rate charge carrier transport, demonstrating the advantages of combining donor and acceptor units within the framework.<sup>55</sup> Charge carrier mobility of  $1.51 \times 10^{-4} \text{ cm}^2 \text{ V}^{-1} \text{ s}^{-1}$  under Ar and photocarrier generation yield of  $3 \times 10^{-3}$  were determined using FP-TRMC measurements. TP-Por COF (Table 2) combined HHTP building block with a linear porphyrin linker, giving access to highly defined interdigitated donor-acceptor heterojunctions.<sup>54</sup> Due to the  $\pi$ -stacked columns of the layered 2D COF, electronic interactions between the COF sheets were possible, thus creating a path for hole and electron migration in opposite directions in an oriented thin film. High thermal stability and electrical conductivity have also been achieved with tetra(*p*-boronic acid phenyl)porphyrin in combination with tetrahydroxyanthracene building block.<sup>77</sup>

Another approach to expand the versatility of chemical reaction routes used for forming COFs as well as to enhance their structural diversity is to use multiple-condensation systems, where one knot and two or three linkers give access to hexagonal and tetragonal multiple-component COFs.<sup>78</sup> This way, multiple-component electron donor-acceptor systems have been achieved, such as those shown in Fig. 5.



**Fig. 5.** Two examples of multiple-component COFs.<sup>78</sup>

HHTP has also been employed as donor in conjunction with naphthalenetetracarboxylic acid diimide (NDIDA) and its pyromellitic derivative (PyrDIDA), resulting in D<sub>TP</sub>-A<sub>NDI</sub>-COF and D<sub>TP</sub>-A<sub>PyrDI</sub>-COF, respectively.<sup>79</sup> Both structures are formed by periodically aligned columnar triphenylene-on-triphenylene and diimide-on-diimide arrays. Steady-state electronic absorption spectra revealed that for D<sub>TP</sub>-A<sub>NDI</sub>-COF no clear charge-transfer band was observed, whereas contrarily, the formation of a charge-transfer complex was observed for D<sub>TP</sub>-A<sub>PyrDI</sub>-COF. The differences in charge transfer and charge separation observed for the NDI and PyrDI acceptors highlighted the necessity of appropriate donor–acceptor pairing to obtain efficient structures for optoelectronic and photovoltaic applications. In a similar approach,<sup>80</sup> donor–acceptor MPc structures were synthesized *via* the co-condensation of metallophthalocyanines containing different central metals as donors, including copper, nickel, and zinc, with a variety of different acceptor molecules, such as naphthalene diimide or perylene diimide building blocks (Fig. 6). Time-resolved transient absorption (TA) spectroscopy and electron spin resonance revealed long-lived charge-carrier lifetime, indicating that efficient charge separation at the molecular junctions is possible with these donor–acceptor COFs. Lifetimes reaching up to  $\tau_{CS1} = 4.8 \mu\text{s}$  and  $\tau_{CS2} = 33 \mu\text{s}$  for D<sub>CuPc</sub>-A<sub>PyrDI</sub>-COF were obtained, showing the potential of these materials to serve as active materials in light-harvesting applications.



**Fig. 6.** Structures of donor–acceptor COFs synthesized through the co-condensation of CuPc with diimide acceptor units. Adapted with permission.<sup>80</sup> Copyright (2015) American Chemical Society.

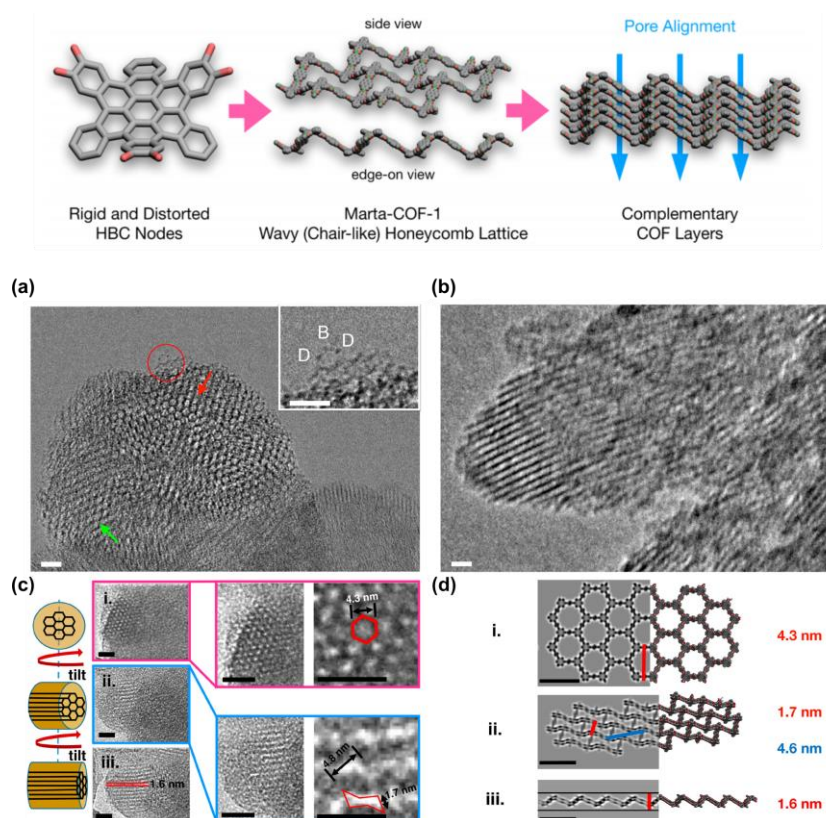
Thiophene-based polymers are commonly used as semiconducting active material in organic photovoltaic devices.<sup>81</sup> However, structural disorder of the donor and acceptor phases in such polymers can limit charge-carrier mobility and charge separation in organic bulk heterojunctions. To overcome these limitations and to obtain deterministic control over the semiconducting segment interactions, the incorporation of thiophene units into COFs has been an attractive goal.

A series of thiophene-containing COFs was synthesized by the co-condensation of HHTP with thiophene-based diboronic acids, such as 2,5-thiophene diboronic acid ( $H_4TDB$ ) and thieno[3,2-*b*]thiophene-2,5-diboronic acid ( $H_4TTDB$ ) (for examples, see Table 2), leading to T-COF-1–4.<sup>56</sup> Interestingly, using  $H_4TDB$  as building block, co-condensation with HHTP leading to boronate ester linked T-COF-1 was only possible under the strict exclusion of water and 3:2 ratio of the diboronic acid and HHTP. Deviations from these conditions resulted in mixed products, where the diboronic acid units formed boroxine rings that subsequently co-condensed with HHTP to give access to T-COF-2. Several thiophene-based COF structures, *e.g.* based on thieno[2,3-*b*]thiophene,<sup>57</sup> benzo[1,2-*b*:4,5-*b'*]dithiophene,<sup>59</sup> and ethoxy-functionalized benzo[1,2-*b*:4,5-*b'*]dithiophene,<sup>62</sup> have been studied in the context of photovoltaics (see section 2.7.4).

Duhović and Dincă described the effect of incorporating heteroatoms such as S, Se, and Te into COFs by using benzodithiophene and the respective heavier chalcogen analogs as building blocks with HHTP to give 1-S, 1-Se, and 1-Te COFs.<sup>63</sup> Pressed pellets of the materials revealed that the electrical conductivity, measured with a two-point probe setup, increased by a factor of two for the Se-containing COF ( $8.4 \times 10^{-9} \text{ S cm}^{-1}$ ) and nearly by a factor of three for the Te-based COF ( $1.3 \times 10^{-7} \text{ S cm}^{-1}$ ) as compared to thiophene ( $3.7 \times 10^{-10} \text{ S cm}^{-1}$ ). Later, Bein, Medina and co-workers reported a highly crystalline DPP2-HHTP-COF consisting of diketopyrrolopyrrole bithiophene and HHTP building blocks. The DPP2-HHTP-COF revealed high electrical conductivity compared to other boronate ester COFs of up to  $2.2 \times 10^{-6} \text{ S cm}^{-1}$ .<sup>64</sup> In addition, the DPP2-HHTP-COF features intriguing optical properties including strong absorption over the visible spectral range, broad emission into the NIR and a singlet lifetime of over 5 ns attributed to the formation of molecular stacks with J-type interactions between successive DPP building blocks in the COF scaffold.

In terms of possible applications for COFs not only optical or electronic properties of the building blocks play an important role but also structural features can be crucial for certain applications. To this end, curvature in the COF structure can give access to new architectures and properties, such as chirality, high surface areas, or enhanced charge-carrier mobilities.<sup>82</sup> Cyclotricatechylene (CTC) has been used as building block with BDBA to obtain undulated 2D CTC-COF (Table 3).<sup>68</sup> Interestingly, the bowl-shaped core unit of the COF led to a larger surface area as compared to its planar analogue COF-5, resulting in higher hydrogen uptake owing to its wavy structure and despite its smaller pore volume. The series of CTC-COFs was later expanded by co-condensing CTC with 4,4'-biphenyldiboronic acid (BPDA) and PDBA to yield CTC-COF-2 and CTC-COF-3, respectively.<sup>68,70</sup> Both COFs featured smaller pore size distributions compared to their planar analogues COF-10 and TP-COF, which was attributed to the curved twisted structure of the respective CTC-COFs.

A wavy 2D COF structure based on core-twisted hexabenzocoronene (HBC) was recently reported by Melle-Franco, Khlobystov, Mateo-Alonso, and co-workers (Fig. 7).<sup>82</sup> The high order of the structure was attributed to the self-complementary concave-convex nature of the building block, which gave access to chair-like honeycomb facets and aligned mesoporous channels. Moreover, a full 3D analysis by transmission electron microscopy (TEM) was carried out from both face-on and edge-on perspective, confirming the presence of both free-standing individual chair-like hexagons as well as zigzag and armchair edges. Furthermore, using TEM tomography the correlations between the observed hexagons, the channel cross sections, and chair-like features of the COF were indicated. Interestingly, no disruption of the interlayer  $\pi$ - $\pi$  stacking was observed as a result of the twisted nature of the framework.

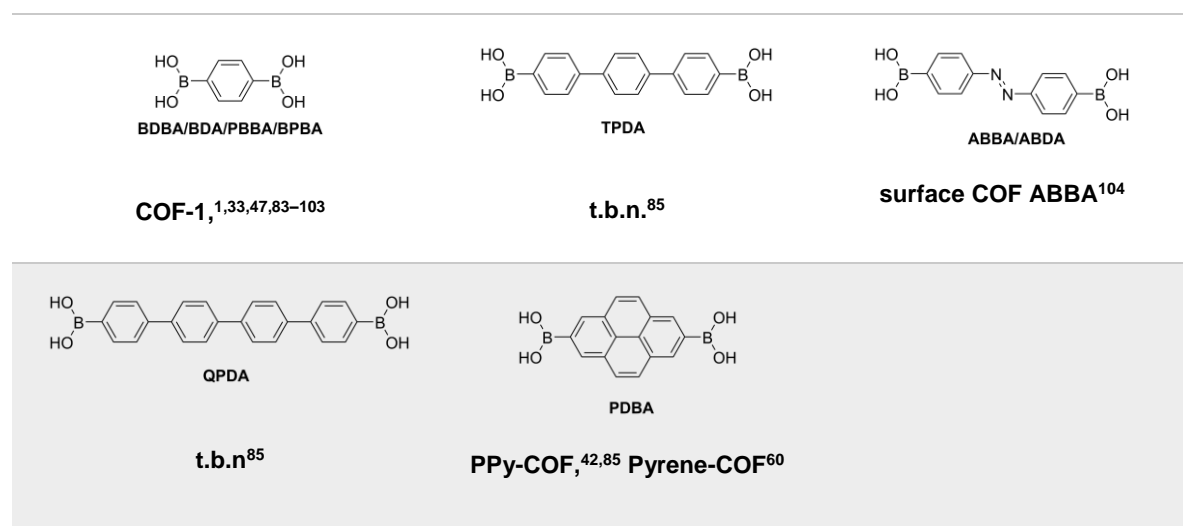


**Fig. 7.** Schematic representation of the rigid and distorted HBC nodes and incorporation into Marta-COF-1. HR-TEM images of highly crystalline domains of the COF are shown: (a) face-on and (b) edge-on (scale bars 10 nm).

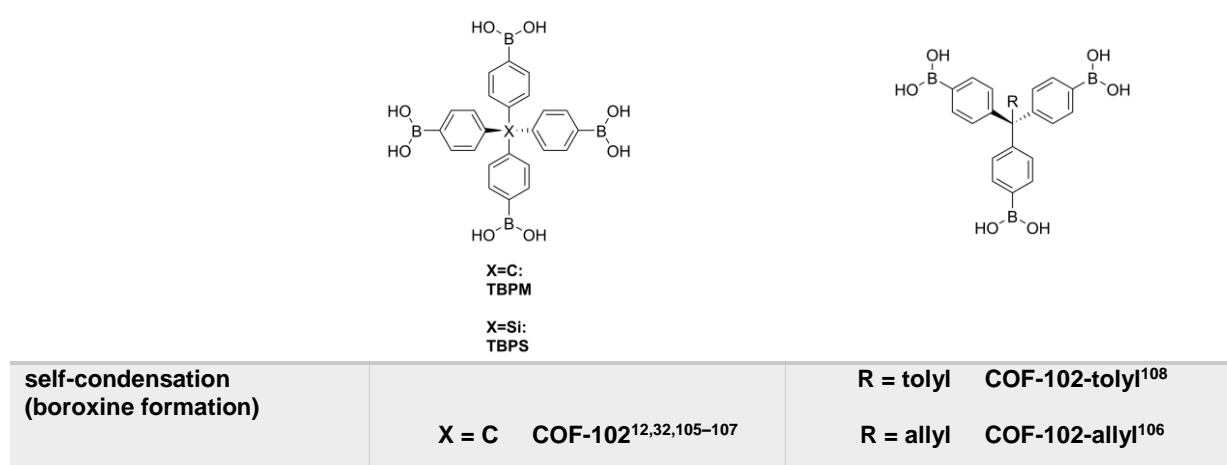
(c) HR-TEM images showing the COF particle rotated and imaged at 70° tilt angle within the plane of the page (panels i–iii) (scale bars 10 nm). (d) Merged quantitative scanning transmission electron microscopy (QSTEM) HR-TEM simulations (left) with the respective geometry-optimized models (right) in face-on (i), chair-like (ii), and edge-on (iii) configuration (scale bars 5 nm). Adapted with permission.<sup>82</sup> Copyright (2019) American Chemical Society.

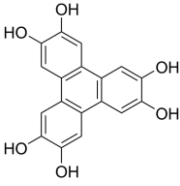
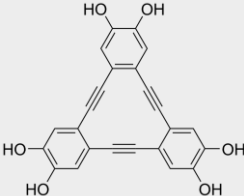
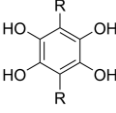
Although some examples of 3D boronic-acid-derived COFs have been reported (Table 5), they remain significantly rarer compared to the related 2D structures. The first 3D COFs were synthesized by Yaghi and co-workers by the combination of triangular and tetrahedral nodes *via* the self-condensation of tetrahedral TBPM and its silicon-derivative tetra(4-dihydroxyborylphenyl)silane (TBPS), giving access to boroxine-linked COF-102 and COF-103, respectively, both of **ctn** topology.<sup>12</sup> Additionally, COF-105 (**ctn**) and COF-108 (**bor**) have been obtained by co-condensation of HHTP with TBPM or TBPS, respectively. All structures showed high thermal stabilities, high surface areas, up to 4210 m<sup>2</sup> g<sup>−1</sup> for COF-103, as well as extremely low densities (for the simulated structures of selected 3D COFs, see Fig. 8). High surface area of 5083 m<sup>2</sup> g<sup>−1</sup> has also been reported for DBA-3D COF (**bor**), which features the DBA[12] building block, opening access to the possibility of incorporating a metal within the DBA cavity (Table 5).<sup>44</sup> High uptake of ethane and ethylene gas was observed for this COF.

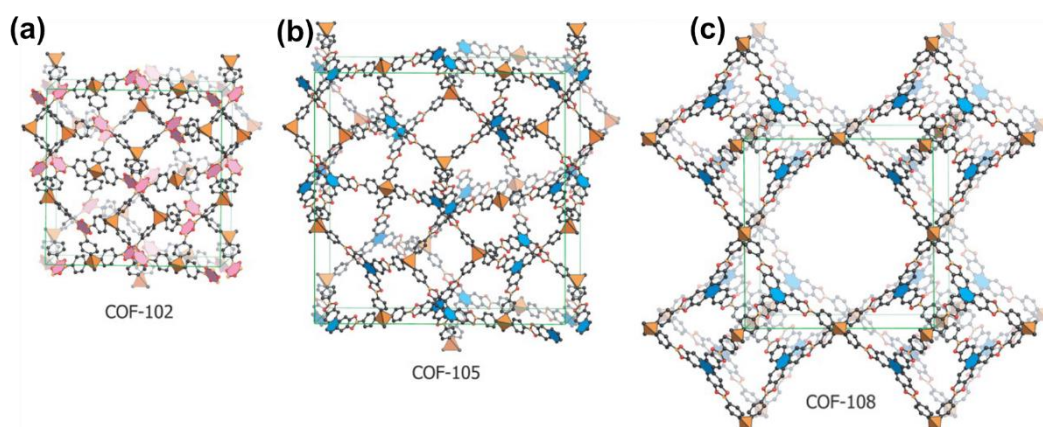
**Table 4.** Boroxine-based COFs. t.b.n = to be named.



**Table 5.** 3D boronate ester COFs.



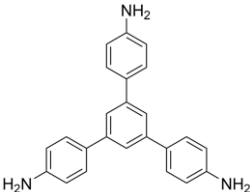
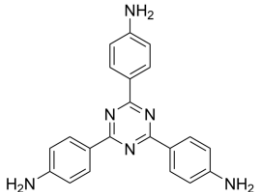
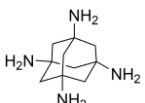
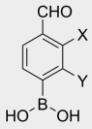
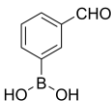
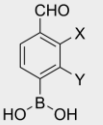
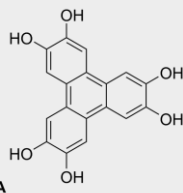
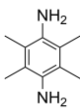
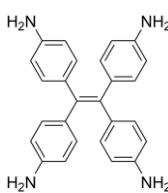
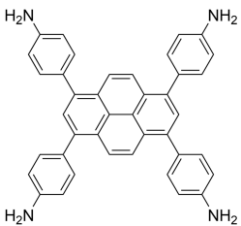
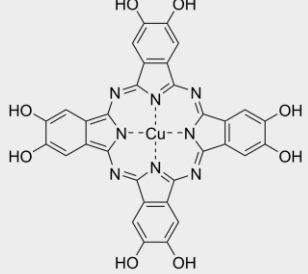
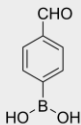
	<b>X = Si</b> <b>COF-103</b> <sup>12,105</sup>	<b>R = -(CH<sub>2</sub>)<sub>11</sub>-CH<sub>3</sub></b> <b>COF-102-C<sub>12</sub></b> <sup>106</sup>
 <b>HHTP</b>	<b>X = C</b> <b>COF-105</b> <sup>12,105</sup> <b>X = Si</b> <b>COF-108</b> <sup>12,105</sup>	
 <b>DBA[12]/AEM-1</b>	<b>X = C</b> <b>DBA-3D-COF</b> <sup>144</sup>	
 <b>R = H: THB</b>	<b>X = C</b> <b>MCOF-1</b> <sup>109</sup>	



**Fig. 8.** Structure and connectivity of different 3D COFs based on PXRD and modeling. (a) COF-102, (b) COF-105, and (c) COF-108. Adapted with permission.<sup>12</sup> Reprinted with permission from AAAS.

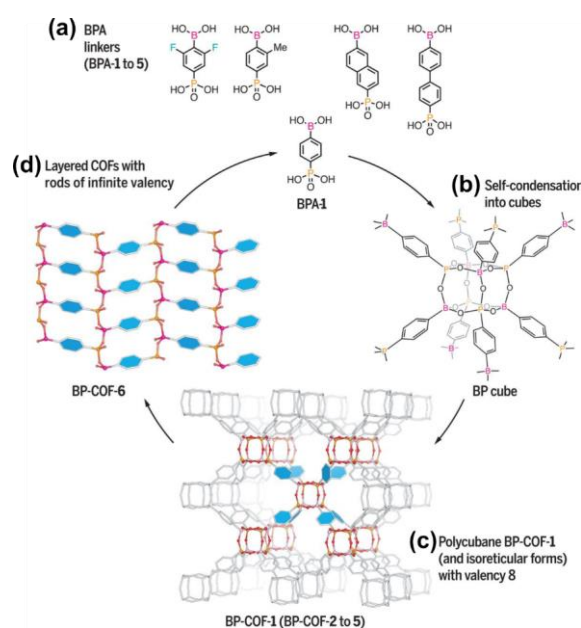
To expand the versatility and structural diversity and to overcome limitations rising from the availability of only a few chemical reactions suitable for COF synthesis, the development of new approaches and reaction systems is a crucial task. To this end, double-stage connection approaches using two types of covalent bonds have been reported, featuring both an imine bond and a boronate ester or boroxine linkage, leading to COFs with enhanced structural complexity and diversity (Table 6). These materials have revealed high surface areas as well as high hydrogen adsorption capacity,<sup>110,111</sup> and the obtained materials feature pore geometries ranging from hexagonal (NTU-COF-1<sup>110</sup>) and tetragonal (e.g. CuPc-FPBA-ETTA COF<sup>111</sup>) to 3D structures (DL-COF-1 and DL-COF-2<sup>112</sup>). Interestingly, as compared to boroxine linked COFs, such hybrid COF structures, such as sCOFA (Table 6), have been reported to feature higher stability,<sup>113</sup> with retention of high crystallinity of the material even after storage under ambient conditions for 20 days.

**Table 6.** Prepared COFs with a double linkage motif.

<div></div> <div>TAPB/ Tab/ TPB/ 3PB/ TPBA</div>	<div></div> <div>TAPT/ TATTA/ Tta/ TT-amine/ TTA</div>	<div></div> <div>TAA</div>	
<div></div> <div><div><div>X = H, Y = H</div><div>X = F, Y = H</div><div>X = H, Y = F</div><div>X = F, Y = F</div></div><div><div>4FPBA/ FPBA</div><div>FFPBA</div><div>FFPBA</div><div>DFFPBA</div></div></div>	<div>X = H, Y = H</div> <div>NTU-COF-1<sup>110</sup></div> <div>X = H, Y = H</div> <div>sCOFA<sup>113</sup></div>	<div>X = H, Y = H</div> <div>TATTA-FPBA COF<sup>111</sup></div> <div>X = F, Y = H</div> <div>TATTA-FFPBA COF<sup>111</sup></div> <div>X = F, Y = F</div> <div>TATTA-DFFPBA COF<sup>111</sup></div>	<div>X = H, Y = H</div> <div>DL-COF-1<sup>112</sup></div> <div>X = H, Y = F</div> <div>DL-COF-2<sup>112</sup></div>
<div></div> <div>3FPBA</div>	<div>sCOFB<sup>113</sup></div>		
<div><div><div><div>X = H, Y = H</div><div>X = F, Y = H</div><div>X = F, Y = F</div></div></div><div><div>4FPBA/ FPBA</div><div>FFPBA</div><div>DFFPBA</div></div><div></div><div>HHTP/ TP</div></div>	<div>X = H, Y = H</div> <div>NTU-COF-2<sup>110</sup></div>	<div>X = H, Y = H</div> <div>HHTP-FPBA-TATTA COF<sup>111</sup></div> <div>X = F, Y = H</div> <div>HHTP-FFPBA-TATTA COF<sup>111</sup></div> <div>X = F, Y = F</div> <div>HHTP-DFFPBA-TATTA COF<sup>111</sup></div>	
	<div></div> <div>TMBDA</div>	<div></div> <div>ETTA/ 4PE</div>	<div></div> <div>Py/ PyTTA</div>
<div></div> <div>CuPc[OH]<sub>8</sub>/CuPc</div> <div></div> <div>3FPBA</div>	<div>CuPc-FPBA-TMBDA</div> <div>COF<sup>111</sup></div>	<div>CuPc-FPBA-ETTA COF<sup>111</sup></div>	<div>CuPc-FPBA-PyTTA</div> <div>COF<sup>111</sup></div>

COFs are typically limited to lower valencies of 3 and 4 as a result of  $sp^2$ - and  $sp^3$ -hybridization of the light element. Very recently, the diversity of COFs was expanded using the concept of higher valency,<sup>114</sup>

where valency of 8 was introduced using building blocks with phosphonic acid groups (Fig. 9). The synthesis of BP-COF-1 is based on a molecular dehydration reaction, in which eight borophosphonic acid BPA-1 linkers react to form a cubic borophosphonate node under elimination of eight water molecules per cube. The generality of the concept was shown using BPA-linkers 2–5 to obtain a series of related COFs (Fig. 9a). Addition of aqueous concentrated HCl to a reaction mixture containing BPA-1 resulted in the formation of a new crystalline phase of large single crystals with infinite-rod topology (Fig. 9d), where the cubic borophosphonates were replaced by infinite 1D B–O–P rods of alternating tetrahedral boron and phosphorus building units connected by phenyl groups with an interlayer spacing of 5.47 Å.



**Fig. 9.** (a) BPA linkers 1–5 with two different functionalities (boronic acid and phosphonic acid groups); (b) and (c) self-condensation of BPA-1 to form BP cubes with a valency of 8, (c) and the resulting polycubane BP-COF-1. (d) Upon addition of acid, BP-COF-1 rearranges to form layered BP-COF-6 with infinite rod valency. Reprinted<sup>114</sup> with permission from AAAS.

## 2.5. Post-synthetic modification of boronic-acid-derived COFs

Post-synthetic modification (PSM) of COFs allows to systematically modify the pore chemical environment in a bottom-up approach<sup>31</sup> by converting further functional groups or by incorporating metals on the building blocks after COF formation.<sup>115</sup> This approach enables the introduction of a wide range of functional moieties into the COF structures and minimizes the involvement of undesired side reactions during reticulation. Thus, a careful design of the post-synthesis scheme is required, where the integrity of the COF structure is maintained during the process.

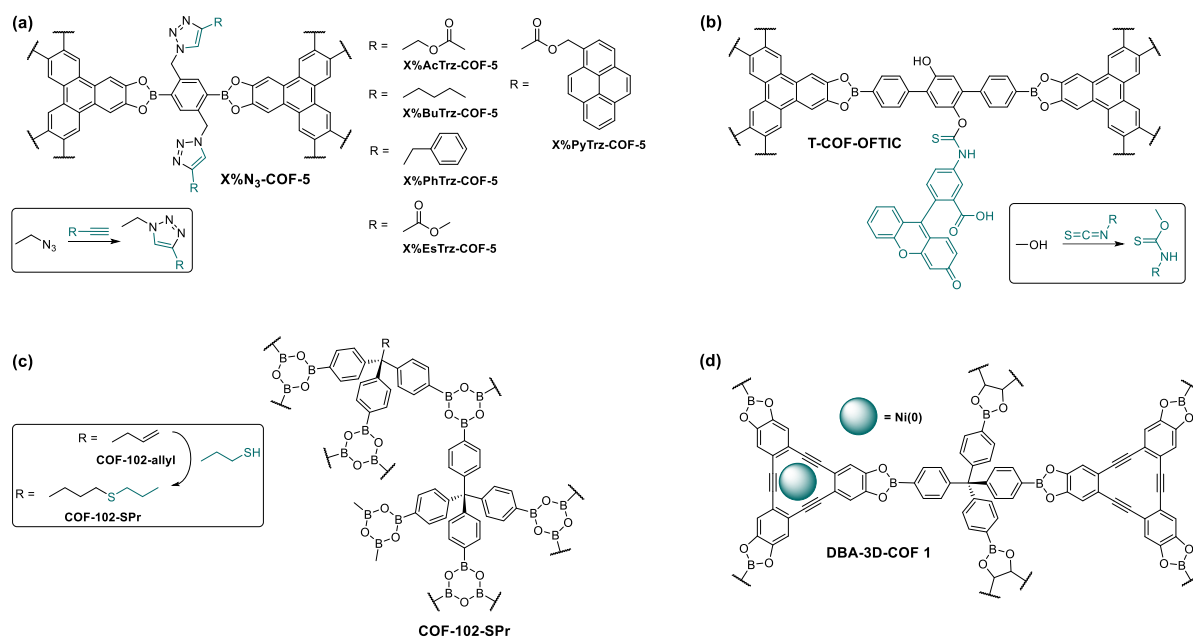
Using the post-synthetic route, boroxine and boronate ester COFs have been modified through several strategies, such as metal incorporation, covalent-bond formation, and monomer truncation.<sup>116</sup> The most common reactions for pore-wall modifications are addition and substitution reactions. The first PSM of COFs by covalent-bond formation was demonstrated by employing azide–alkyne cycloaddition.<sup>117</sup> To tune the density of the wall-anchored groups, a mixed-linker strategy was employed, in which a mixture of azide-functionalized benzenediboric acid (N<sub>3</sub>-BDBA, Scheme 5a) and BDBA was converted with

HHTP to boronate ester X%N<sub>3</sub>-COF-5 (X = 5, 25, 50, 75, and 100). Subsequently, the COFs were functionalized through click chemistry by various alkynes containing long alkyl chains, polar ester groups, and pyrene in quantitative yields. This approach has also been used to functionalize Pc-containing boronate ester N<sub>3</sub>-NiPc-COF and donor–acceptor [C<sub>60</sub>]<sub>y</sub>-ZnPc-COF,<sup>118</sup> the latter having phthalocyanine as an electron donor and fullerene as an electron acceptor.

Hydroxyl groups have been used as anchoring sites for PSM of COFs due to their small size, diverse reactions with other functional groups, and great variety of available linker molecules. Medina, Bein, and co-workers<sup>52</sup> synthesized hydroxyl-functionalized mesoporous boronate ester T-COF-OH (Scheme 5b), which was post-synthetically labeled with fluorescein-isothiocyanate (FTIC) by forming *o*-thiocarbamate bonds. The fluorescent dye allowed for the visualization of the material in a fluorescence microscope, confirming the successful PSM reaction.

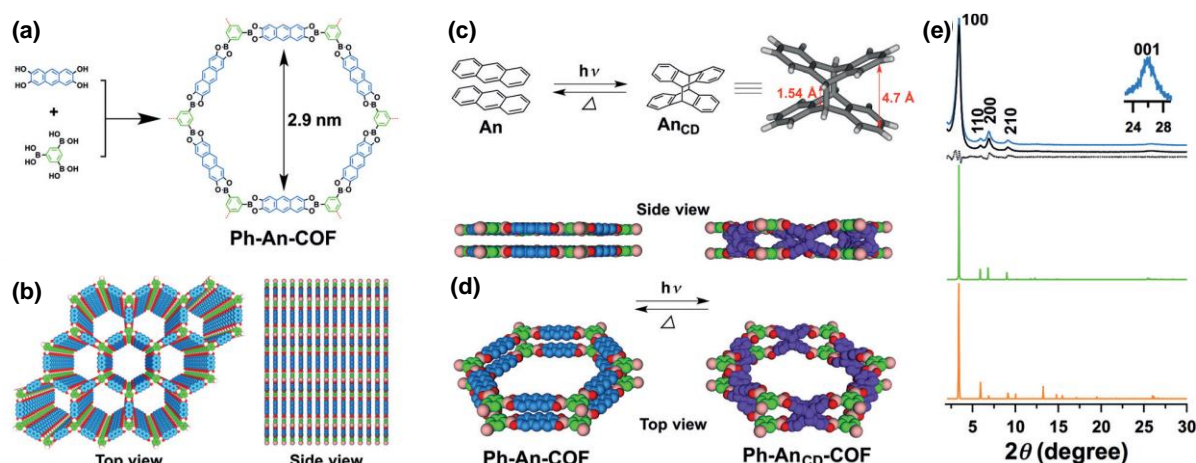
Monomer-truncation strategy was employed for the functionalization of boroxine-linked 3D COF-102.<sup>106</sup> Tetrahedral TBPM building block was modified by replacing one of its four arylboronic acid groups with a dodecyl or an allyl functional group. The co-condensation of the modified TBPM linkers with pristine TBPM led to boroxine-linked 3D COF-102-C<sub>12</sub> and COF-102-allyl structures, respectively. High loading levels of >30% of the truncated building blocks still resulted in crystalline COF structures with high surface areas. In a similar approach, tolyl-functionalized COF-102 was formed by the co-condensation of 4-tolylboronic acid and TBPM.<sup>108</sup> The PSM<sup>119</sup> of COF-102-allyl was carried out under typical thiol–ene reaction conditions by adding propanethiol to a solution containing a photoinitiator and COF-102-allyl. The resulting thio-modified COF-102-SPr (Scheme 5c) retained the long-range order and identical **ctn** network topology with COF-102-allyl.

The regular structure of COFs provides a platform for uniform ligand distribution with catalytically active metals throughout the structures, allowing for the effective isolation of the active sites of the catalyst.<sup>116</sup> Different metals have been incorporated into COFs in the form of inorganic salts taking advantage of metal–ligand interactions. McGrier and co-workers<sup>120</sup> metalated a mesoporous 3D COF prepared from C<sub>3</sub>-symmetric  $\pi$ -electron conjugated triangular DBA (Scheme 5d) and four-fold symmetric TBPM building blocks. Treatment of the COF with a nickel complex resulted in a material with 10 wt% of Ni, with retention of COF crystallinity and minimal reduction of surface area.



**Scheme 5.** PSM approaches for the synthesis of (a)  $X\%N_3\text{-COF-5}$ ,<sup>117</sup> (b)  $T\text{-COF-OFTIC}$ ,<sup>52</sup> (c)  $\text{COF-102-SPr}$ ,<sup>106</sup> and (d)  $\text{DBA-3D-COF 1}$ .<sup>120</sup>

An elegant approach to modify the COF skeleton COFs was demonstrated using cycloaddition reaction. A photoresponsive anthracene unit was used with BTBA (Table 3) to synthesize a structurally dynamic boronic ester Ph-An-COF (Fig. 10).<sup>13</sup> The anthracene columns in the COF were situated in eclipsed stacking mode with an interlayer distance of 3.4 Å, which is favorable for photoinduced  $[4\pi+4\pi]$  cycloaddition reactions. Thus, irradiation of Ph-An-COF films induced the cycloaddition reaction of the anthracene units forming concave-convex shaped dimers. The dimerization resulted in drastic conformational changes in the COF backbone and triggered a structural transformation of layers (Fig. 10d). The XRD pattern of the modified COF was similar to that of Ph-An-COF but with decreased reflection intensity, which was attributed to the relatively flexible conformation of concave-convex skeletons. The cycloaddition reaction was thermally reversible, and heating regenerated the planar anthracene units and the Ph-An-COF structure. The structural transformations led to profound changes in the properties and functions, including gas adsorption, photo-absorption, and luminescence.



**Fig. 10.** (a) Synthesis of  $\text{Ph-An-COF}$ . (b) Top and side views of  $\text{Ph-An-COF}$ . (c)  $[4\pi + 4\pi]$  Cycloaddition upon irradiation, the formation of the dimer, and thermal reversibility of the reaction. (d) Side and top views of the structural transformation. (e) XRD patterns of  $\text{Ph-An-COF}$  and  $\text{Ph-An}_{\text{CD}}\text{-COF}$ .

changes of the COF upon photoirradiation and thermal stimulation. (e) XRD patterns of Ph-An-COF: experimentally observed (blue curve), Pawley refined (black curve), their difference (dotted curve), and the patterns simulated using the eclipsed AA (green curve) and staggered AB (orange curve) stacking modes. Reprinted with permission.<sup>13</sup>

## 2.6 Processing

Typically, COFs are obtained as insoluble microcrystalline powder precipitates from reactive precursor solutions. This feature imposes a great challenge for their processing and surface growth. To enable the utilization and performance assessment of COFs for applications, particularly as functional devices, developing synthesis routes that provide ordered COF-on-surface deposition is essential. In the following we will briefly present different methodologies developed for the preparation of colloidal COF particles and thin films.

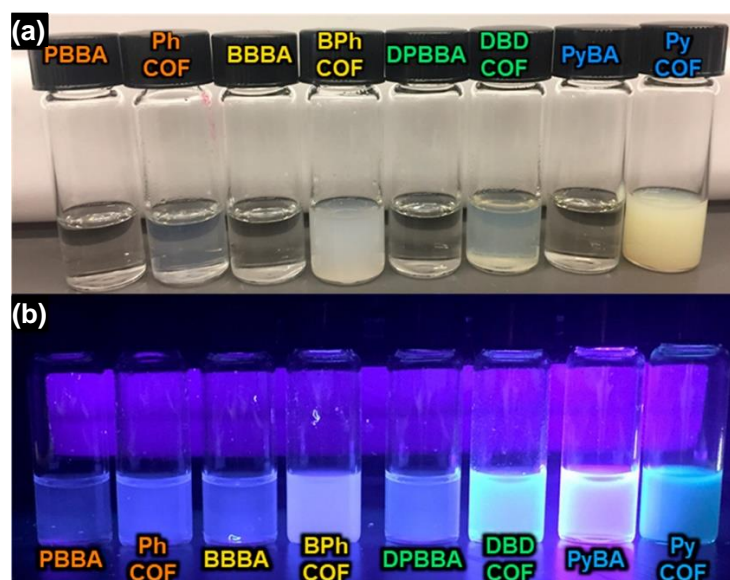
### 2.6.1 Colloidal COFs

One route to gain control over the COF growth process is aiming at limiting the fast precipitation of agglomerated COF crystallites, namely stabilizing COF particle suspensions. Addressing this challenge, Dichtel and co-workers<sup>121</sup> demonstrated the stabilization of four boronate ester-linked COFs, COF-5, COF-10, TP-COF, and HHTP-DPB COF, as colloidal suspensions by adding nitrile-containing co-solvents to the reaction mixture. Acetonitrile serves as a surface stabilization agent of the COF crystallites by interacting with the boronate linkages to suppress the attractive forces between the crystallites, disrupting the aggregation and precipitation without inhibiting polymerization. For example, in the presence of 55% acetonitrile, crystalline COF-5 was observed within 15 min reaction time with relatively uniform particle size distribution. Mean radius of 21 nm at 25 min and 30 nm at 2 h was determined by line broadening calculation of the SAXS data using the Scherrer equation. The particle sizes of these COFs were comparable to the 20–40 nm crystallite sizes of COF-5 precipitates prepared in the absence of acetonitrile and determined by X-ray diffraction.<sup>34</sup> At a longer reaction time of 20 h at 90 °C, the average particle size of the COFs synthesized with varying monomer and acetonitrile concentrations was measured by dynamic light scattering (DLS). Stable colloidal COF particles with average sizes of 240 nm, 100 nm, and 45–60 nm were observed with acetonitrile concentrations of 15, 35, and >55 vol%, respectively. With acetonitrile concentrations >55 vol%, the average size was relatively invariant, being comparable to the 20–40 nm crystalline domains of precipitated COF-5 powders. After colloid formation, particle sizes were not affected by dilution with non-nitrile solvents or by exposure to different acetonitrile concentrations, even at elevated temperatures. This synthesis approach provides stable colloidal COF suspensions when acetonitrile is used at volume fractions of 15–95%. Interestingly, the COF suspensions were reported to be stable for several weeks at room temperature with no apparent precipitation (*i.e.* particle aggregation).

The ability to obtain well-dispersed colloidal COF solutions has also allowed access to single-crystalline boronate ester-linked<sup>41</sup> and boroxine-linked<sup>122</sup> COFs. Controlled COF formation was studied using a two-step approach, in which the nucleation and growth processes are essentially separated, resulting in three boronate ester single-crystal 2D COFs: COF-5, COF-10, and TP-COF. First, using acetonitrile as co-solvent, crystalline COF colloids with an average diameter of 30 nm were prepared to serve as

seeds for the growth of larger crystals. Slow addition of monomer solutions at 0.10 equiv./h to the existing colloidal COF crystals allowed for crystal growth without the formation of new nuclei, whereas the opposite was found for fast addition at 1.0 equiv./h, eventually leading to a large particle size distribution. HR-TEM showed that the obtained COF-5 particles have six-fold symmetry and hexagonal faceting in projection along the *c*-crystal axis. The singled-out COF-5 crystals were between 300 and 500 nm in diameter.

The well-dispersed, single-crystalline COF colloids enabled the characterization of their photophysical properties by TA spectroscopy.<sup>123</sup> An improved signal quality of three orders of magnitude in comparison to polycrystalline powders was found, enabling the study of excited state dynamics and optical signatures of COF crystals. The studies revealed that excitons in smaller COF particles undergo exciton–exciton annihilation more easily due to their confinement to smaller effective volume in comparison with larger particles. In a later study,<sup>122</sup> the synthesis of large COF crystallites was expanded to boroxine-linked colloidal frameworks including four 2D (Ph-COF, BPh-COF, Py-COF, DBD-COF) and one 3D COF (TPh-COF) (Fig. 11). The syntheses were carried out under solvothermal conditions in the presence 50 vol% of acetonitrile. Colloidal stabilization enabled detailed structural analysis by HR-TEM, and an investigation of the optoelectronic nature of these materials with excitation–emission matrix fluorescence spectroscopy (EEMS). The EEMS studies of PPy-COF, for example, indicated the formation of J-aggregates and excited charge-transfer complexes, where interlayer pyrenes are in proximity through the COF matrix. Additionally, colloidal COF solutions were used for the synthesis of free-standing transparent COF films<sup>121</sup> and the preparation of spray-coated 2D COF thin films.<sup>124</sup> For further details, see sections 2.6.2 and 2.7.5.



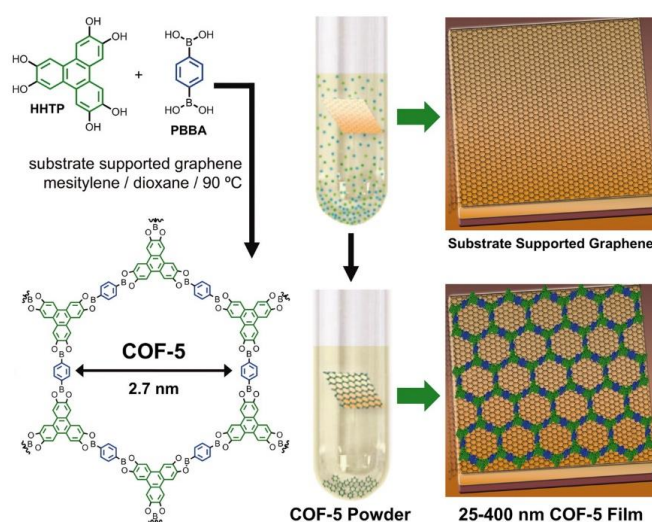
**Fig. 11.** COF monomer solutions and the respective COF nanocrystal suspensions (a) under natural light and (b) under UV irradiation. Reprinted with permission.<sup>122</sup> Copyright (2019) American Chemical Society.

An alternative synthetic method to prepare boronate-ester-linked colloidal COFs was realized in the presence of a monofunctional modulator, TCAT, a capping agent, which suppresses the nucleation but permits seeded growth.<sup>119</sup> The inhibition of colloid nucleation is concentration dependent, where TCAT loadings of 0–5 equivalents failed to suppress nucleation, resulting in large particles, whereas the

presence of 10 and 15 equivalents of TCAT resulted in the formation of colloidal COF suspensions. To expand the size of the existing 2D COF colloidal seeds, 15 equivalents of the TCAT modulator with varying amounts of COF building blocks were added to the suspension, showing an increase in crystallinity and particle size over the course of 2 days. Varying the monomer concentration from 0 to 4.5 equivalents relative to that present in the initial colloids resulted in an average particle size increase from 60 to 450 nm, respectively, in 2 days. TEM studies of the COF colloids grown in the presence of TCAT confirmed that the colloids primarily expand vertically by oriented attachment of oligomers in the out-of-plane direction.

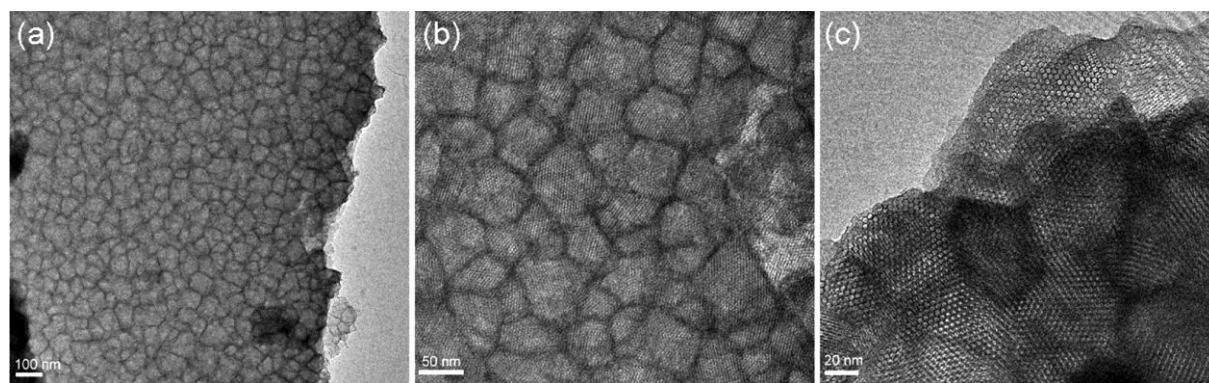
## 2.6.2 Thin Films

The first COF thin films were obtained under solvothermal conditions, where COF powders and films were produced simultaneously in the same reactor using the so-called *in situ* approach. The inclusion of single-layer graphene (SLG) modified surfaces in the reaction mixture, which served as a preferred site for film nucleation, allowed for epitaxial growth of COF films (Fig. 12).<sup>125</sup> Oriented 2D COF thin films on SLG of COF-5, TP-COF (Table 2), and NiPc-PBBA COF were prepared supported by several different substrates, such as polycrystalline Cu films on Si wafers (SLG/Cu), fused SiO<sub>2</sub> (SLG/SiO<sub>2</sub>), or SiC (SLG/SiC). All resulting films were crystalline and oriented with the 2D aromatic molecular planes stacked perpendicular to the SLG surface with full coverage of the surface. To evaluate the photophysical properties, COF films grown transparent fused SLG/SiO<sub>2</sub> as substrate material were employed, enabling UV/Vis/NIR spectroscopy. The same approach was used to prepare oriented thin films of HHTP-DPB COF (Table 2) on SLG on a transparent fused SiO<sub>2</sub> substrate.<sup>51</sup> Later, Dichtel and co-workers monitored the growth of ZnPc-based COF thin films on SLG-modified fused SiO<sub>2</sub>, where the crystallite orientation in the film was strongly dependent on the solvents used for the synthesis.<sup>74</sup> Solvent mixture of DMAc/*o*-dichlorobenzene (DCB) led to crystalline but unoriented films, whereas dioxane, MeOH, DMA, and DCB in 3:1:2:1 (v/v) ratio resulted in the formation of oriented and crystalline films.



**Fig. 12.** An illustration of the solvothermal synthesis of COF thin films on substrate-supported graphene. Co-condensation of HHTP and PBBA leads to both COF-5 powder as well as film on the graphene surface. Reprinted<sup>125</sup> with permission from AAAS.

Using solvothermal conditions, Medina et al.<sup>59</sup> demonstrated the non-epitaxial synthesis of oriented COF films on SLG-free substrates, such as transparent conductive oxides (TCO), i.e. indium-doped tin oxide (ITO), gold substrates, and even fused silica, and an example for amorphous substrates. Thin films of BDT-COF (Table 3) were synthesized in a bottom-up approach using a stainless-steel autoclave equipped with a Teflon liner and substrate holder. The substrates were placed horizontally on the substrate holder allowing them to be suspended in the reactive precursor solutions. In this way, thin, porous, and highly oriented BDT-COF films were obtained (Fig. 13), grazing incidence diffraction (GID) measurements of which revealed the preferential horizontal alignment of the 2D COF sheets relative to the substrate. Furthermore, halting the film synthesis reaction at 2 h revealed films consisting of free-standing pillars in close vicinity of each other, indicating island-growth mechanism with crystal domain sizes in the c-direction being smaller than those obtained at longer reaction times. In addition, the ability of the electron donor BDT-COF to host an electron acceptor phase in the oriented COF channels was investigated by TA measurements, which indicated the stabilization of hole-polaron charge carriers at the COF backbone, featuring elongated life-time upon inclusion of an electron-accepting phase.



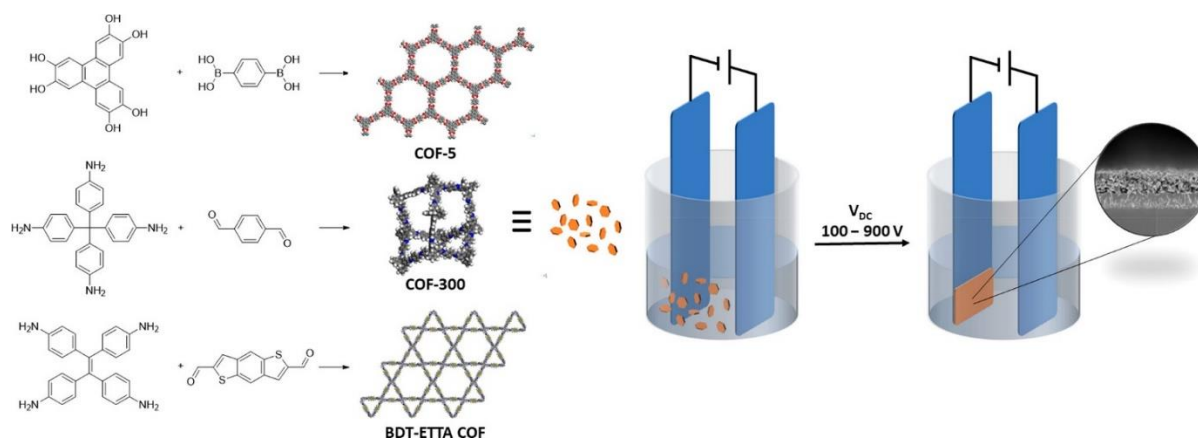
**Fig. 13.** TEM micrographs of BDT-COF thin film fragment grown on a gold surface showing the hexagonal structure along the c-axis at different magnifications. Reprinted with permission.<sup>59</sup> Copyright (2014) American Chemical Society.

Boronate ester and boroxine COF films and powders have also been shown to form under mild conditions through vapor-assisted conversion (VAC) at room temperature.<sup>60</sup> In the VAC procedure, a COF precursor solution was drop-casted on a substrate, such as glass, TCOs, or gold, providing a thin reactive layer solution. The substrates were then placed in a desiccator equipped with a small vessel containing mesitylene and dioxane for 72 h. In due course, evenly covered, porous, and highly crystalline films of BDT-COF (Table 2), COF-5 (Table 2), and PPy-COF (Table 4) were obtained with a precise thickness, controlled by the amount of the precursor solution deposited on the substrate, ranging from a few hundred nanometers to several microns. The film morphology was found to be dependent on the film thickness, and thin films of about 300 nm were observed as continuous films, whereas thicker films featured agglomeration of the COF particles with evident textural porosity.

Using continuous flow synthesis, where constant rates of monomer precursor mass was deposited at constant elevated temperatures, crystalline thin films with preferred crystal orientation of COF-5 (Table 2), DPB-COF (Table 2), TP-COF (Table 2), and COF-10 (Table 2) were achieved with a fine control over the film thickness.<sup>126</sup> For the synthesis of COF-5 in a flow-cell, the building blocks HHTP and BDBA

were mixed at 25 °C in a dioxane/mesitylene solvent mixture, after which rising the temperature to 90 °C resulted in the formation of COF-5 after 2 min. The resulting reaction mixture was pumped through a heated tubing for a given residence time and passed through a flow cell over a substrate. The deposited mass was monitored by a quartz crystal microbalance (QCM). High crystallinity of the resulting COF films was observed at longer residence times of 80 and 100 s, indicating that crystalline films are likely to form through the addition of larger oligomeric species to the substrates rather than monomers. Using the continuous flow method, thicker films (374 nm for DPB-COF) were accessed compared to films obtained by a static film growth (261 nm).

Electrophoretic deposition (EPD, Fig. 14) has been reported by Medina and co-workers for the synthesis of 2D or 3D COF films linked by boronate ester or imine bonds.<sup>127</sup> External electric field induced to a parallel electrode set up immersed in COF-5 nanoparticle suspension of a low dielectric constant solvent, such as ethyl acetate, led to the migration of COF particles, which bear a negative intrinsic surface charge, to the electrode's surface of opposite charge to give a continuous film of gathered crystallites. Notably, the COF particle suspensions were obtained either by a top-down approach by breaking down large agglomerated COF particles by sonication, or re-suspending COF powders in the respective solvents. This way, COF films with an inherent textural porosity were formed on a time scale of minutes. Using EPD, the thickness and the covered surface area of the resulting films was precisely controlled by controlling parameters such as the deposition time, applied potential, and concentration of the COF particles, in a short time scale. For COF-5, in only 2 min a film with 14 µm thickness was obtained. Furthermore, this method also allowed for the co-deposition of different COFs as well as COF/Pt nanoparticles from mixed suspensions.



**Fig. 14.** COF building blocks and the resulting frameworks used for electrophoretic deposition. A schematic representation of the EPD set-up is shown together with a representative cross-section SEM image of the resulting COF thin film. Reprinted with permission.<sup>127</sup> Copyright (2019) American Chemical Society.

Free-standing transparent crystalline and porous COF films with preferential crystallite orientation, where the aromatic planes are positioned perpendicular to the film surface have been reported by solution-casting of stable colloidal suspensions of 2D COF nanoparticles and drying.<sup>121</sup> Such colloidal COF suspensions have also been used as ink for spray coating of 2D COF thin films.<sup>124</sup> Five different boronic-ester-COF-based colloidal inks were spray-coated at high speed, large-scale, and micrometer-scale resolution, either in isolation or as mixtures, onto several substrates, such as metal, polymer, and

oxide substrates, thus allowing not only the formation of pure materials but also film-based devices with mixed 2D COFs.

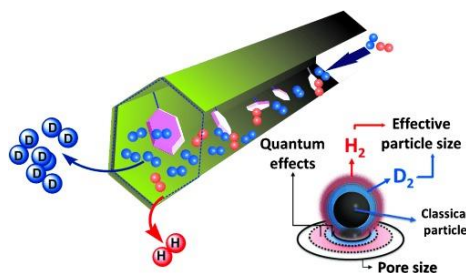
## 2.7 Applications

The high porosity, tunable pore size and structure, and light weight of COFs combined with the immense number of organic molecules render COF materials as a unique platform to design a specific spatial orientation of organic ligands. Therefore, in the literature, boronate ester COFs have been studied for a wide range of applications, such as gas storage, sieving, batteries, and optoelectronics. In the following section, the exploration of boronate ester COFs for different applications will be discussed.

### 2.7.1 Sieving/Separation of Molecules

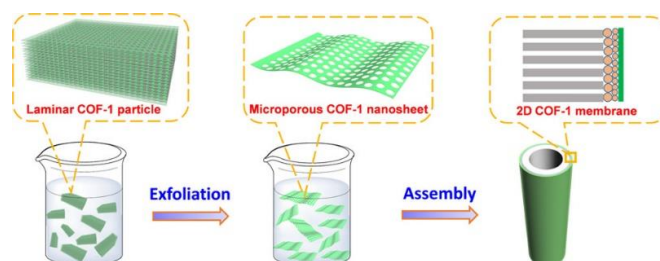
Compared with inorganic zeolites, COFs feature the advantage of providing a more versatile chemical diversity due to the immense number of different organic building units that can be used for their synthesis. Moreover, their properties, such as tunable pore sizes and shapes as well as easily customizable functionalities, make them perfect candidates for application in molecular separation.

The pore wall modification of COF-1 using pyridine (Py) gave access to Py@COF-1, which enabled the separation of isotope mixtures of  $H_2$  by highly selective quantum sieving as described by Oh *et al.*<sup>86</sup> Py@COF-1 was synthesized by Lewis-base-assisted self-condensation reaction of BDDBA in the presence of pyridine. Using this approach, the pore aperture size and the pore volume of Py@COF-1 were significantly decreased compared to the parent COF-1: gas adsorption measurements revealed that neither  $N_2$  at 77 K nor  $H_2$  at 19.5 K could penetrate the structure due to its high density, resulting in BET surface areas of  $20.5 \text{ m}^2 \text{ g}^{-1}$  and  $48 \text{ m}^2 \text{ g}^{-1}$  for  $N_2$  and  $H_2$ , respectively, greatly reduced from that of COF-1 of  $711 \text{ m}^2 \text{ g}^{-1}$ . Interestingly, Py@COF-1 exhibits unique sorption behavior at low temperatures (19.5–70 K). Analyzing the  $H_2$  uptake at different low temperatures, an increase in the surface area from  $20.5 \text{ m}^2 \text{ g}^{-1}$  at 19.5 K to  $250 \text{ m}^2 \text{ g}^{-1}$  at 77 K was observed, indicating framework flexibility with changes in the effective aperture size and gating effects, meaning that already at low temperatures (>30 K) the system showed cryogenic flexibility. Since the cryogenic flexibility produces a kinetic hindrance at the aperture, this allowed for highly size-selective quantum sieving of  $D_2$  from a 1:1  $H_2/D_2$  isotope mixture using Py@COF-1 in a temperature range of 20–100 K (Fig. 15). The different  $H_2$  isotopes display a difference in adsorption strength at low temperatures as a result of a strong isotope effect, which is used in quantum sieving in order to separate the different  $H_2$  isotopes.<sup>128</sup>



**Fig. 15.** Schematic representation of the quantum sieving process of  $D_2$  from a 1:1 mixture of  $H_2/D_2$ . Reprinted with permission.<sup>86</sup> Copyright 2013, John Wiley and Sons.

Homogeneous and ultra-thin COF membranes were obtained from COF nanosheets, where the as-synthesized COF-1 was immersed in dichloromethane and subjected to sonication, resulting in exfoliated COF nanosheets (Fig. 16).<sup>96</sup> Then, a membrane was produced by depositing the COF-1 nanosheet solution onto the outer surface of a macroporous ceramic support. The single-gas permeation study of the membrane for H<sub>2</sub>, N<sub>2</sub>, and SF<sub>6</sub> at 350 °C gave nearly constant rates of permeance, indicating that the membrane was highly stable under high temperatures.



**Fig. 16.** Schematic representation of the fabrication of a COF-1 membrane produced via the exfoliation of COF-1 to nanosheets. Reprinted with permission.<sup>96</sup> Copyright (2017) American Chemical Society.

Graphene oxide (GO)/COF-1 nanocomposite prepared through the *in situ* growth route showed excellent water permeation as membrane material for water treatment.<sup>101</sup> High rejection rates were observed for water-soluble dyes (>99%) and lower rejections for salts (<12%), which was attributed to the physical size sieving of COF-1 and the suitable interlayer spacing between the adjacent GO sheets of 1.03 nm, resulting from the presence of the COF as spacer, making the composite a promising material for the extraction of dyes from wastewater.

Boronic-acid-derived COFs have also been probed as stationary phases for gas and liquid chromatography. COF-5 was grown on the inner wall of a fused silica capillary *via* polydopamine (PDA) supported method, where the catechol moieties of the immobilized dopamine on the surface of the tube served as anchoring sites for the COF growth.<sup>129</sup> The obtained COF-5-PDA@capillary stationary phase was used for open-tubular capillary electrochromatography (OT-CEC) and showed high column efficiencies, stability, and repeatability in baseline separation of neutral, acidic, and basic small organic molecules. For example, baseline separation of ethylbenzene, *n*-propylbenzene, and *n*-butylbenzene was achieved, whereas for the non-COF-containing PDA@capillary no separation was observed, indicating that an interaction between the neutral analytes with the COF-5 layers led to the separation of the three alkyl benzenes. PDA-based functionalization has also been employed to immobilize COF-1 on the surface of magnetic nanoparticles (M-COF-1).<sup>91</sup> Selective extraction of paclitaxel, a known anti-cancer drug in clinical chemotherapy, was carried out using this composite with good linearity in the range of 0.1–200 ng mL<sup>-1</sup> with a low limit of detection of 0.02 ng mL<sup>-1</sup>.

A COF composite based on a CTC-COF shell (Table 3) and magnetic nanoparticles inside carbon nanotubes (MCNT), CTC-COF@MCNT, was employed for magnetic solid-phase extraction (MSPE) of heterocyclic aromatic amines (HAA) from complex food samples.<sup>69</sup> The composite was prepared through a photochemical reaction of MCNT, BDBA, and CTC in dioxane and 3-aminopropyltriethoxysilane (APTES), and featured large specific surface area of 430 m<sup>2</sup> g<sup>-1</sup> and enhanced moisture stability as compared to pristine CTC-COF. Thus, CTC-COF@MCNT was used as

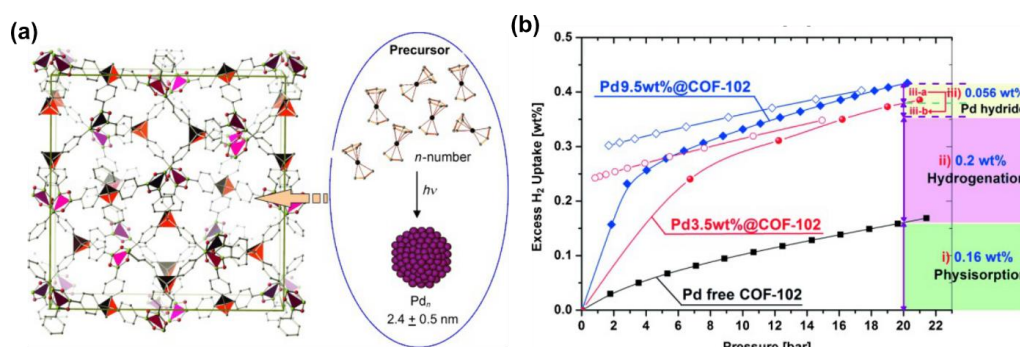
adsorbent for MSPE to enrich HAAs prior to their analysis with ultra-high-performance liquid chromatography-tandem mass spectrometry. To this end, the processed food sample and CTC-COF@MCNT composite were combined, shaken, and after a specific time, the CTC-COF@MCNT composite was separated from the solution using an external magnetic field. HAAs were subsequently desorbed from the adsorbent by addition of methanol, and limit of detection (LOD) of 0.0058–0.025 ng g<sup>-1</sup> and good linearity over the range of 0.05–50 ng g<sup>-1</sup> were obtained.

## 2.7.2 Gas Storage

Porous materials have attracted a great deal of interest as possible storage materials for gases, such as hydrogen, carbon dioxide, methane, or ammonia. The storage of methane and hydrogen is especially important owing to their potential to serve as alternative energy sources, replacing fossil fuels. To this end, the regular pore structures and large surface areas of light-weight COFs are particularly beneficial.

Hydrogen storage was one of the first applications investigated for boronate ester COFs. In a theoretical study, the hydrogen storage properties of a series of 2D and 3D COFs were studied, and the hydrogen storage capacity of 3D COFs was found to be almost three times as high as that of 2D COFs as a result of their higher surface area and free volume,<sup>102</sup> with a maximum H<sub>2</sub> uptake of 18.9 wt% at 77 K calculated for COF-108. In a study by Ghosh *et al.*, using density functional theory (DFT) and grand canonical Monte Carlo (GCMC) simulations, the H<sub>2</sub> adsorption of COF-1 (Table 4), COF-5 (Table 2), and porphyrin-containing H<sub>2</sub>P-COF (Table 3) was theoretically predicted.<sup>72</sup> COF-5 was simulated to have the highest hydrogen adsorption capacity among the analyzed COFs, which was attributed to its high free volume (2.45 cm<sup>3</sup> g<sup>-1</sup>) and the high binding energy of the boronic ester ring. The inclusion of pyridine units inserted between the layers of 2D H<sub>2</sub>P-COF allowed for an increased interlayer spacing and thus enhanced the accessible volume for hydrogen adsorption. The highest storage capacity among the studied 2D COFs was achieved for H<sub>2</sub>P-COF doped with four pyridine molecules with a gravimetric and volumetric uptake of ~5.1 wt% and 20 g H<sub>2</sub>/L at room temperature and 100 bar. The hydrogen storage capacity of COF-1 has also been calculated to be enhanced by decorating the framework with lithium atoms.<sup>99</sup> Ab initio molecular dynamics (MD) simulations showed that six Li atoms were uniformly dispersed on a COF-1 layer and three hydrogen molecules were adsorbed per Li-atom in the Li-COF-1 system. At 300 K, 12 hydrogen molecules were adsorbed on the Li-COF-1 layer, which led to a hydrogen hosting capacity of 5.26 wt%.

Metal species have been included in the COF pores to improve their hydrogen storage ability.<sup>107</sup> The inclusion of ultra-small palladium nanoparticles into COF-102 by photodecomposition of [Pd( $\eta^3$ -C<sub>3</sub>H<sub>5</sub>)( $\eta^5$ -C<sub>5</sub>H<sub>5</sub>)]@COF-102 yielded hybrid material Pd@COF-102, which featured monodispersed Pd nanoparticles in the size of 2.4 nm evenly distributed inside the COF. Hydrogen sorption measurements showed that the inclusion of Pd nanoparticles led to an improvement in the hydrogen hosting capacities by a factor of 2–3 at room temperature and 20 bar (Fig. 17). High hydrogen uptake has also been shown for bowl-shaped CTC-COF, which with 1.12 wt% at low pressure outperformed other 2D frameworks with similar structures (COF-5 0.84 wt%, COF-10 0.82 wt%), owing to its larger surface area.<sup>68,70</sup>

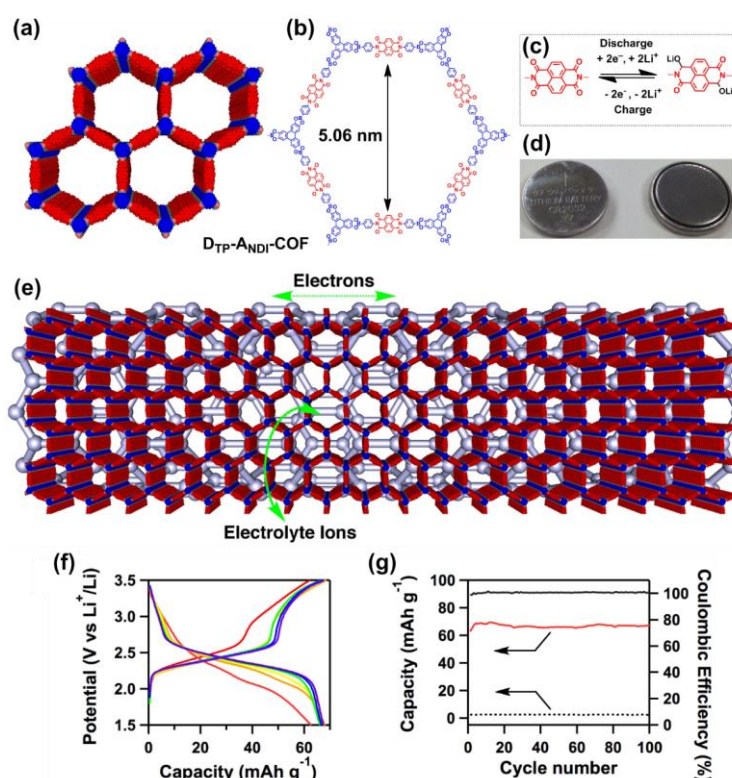


**Fig. 17.** (a) Schematic representation of the synthesis of Pd@COF-102 hybrid material. C, B, and O atoms are depicted in grey, red, and green, respectively. Excess hydrogen storage sorption isotherms of pristine COF-102, Pd3.5wt%@COF-102, and Pd9.5wt%@COF-102 at (b) 298 K. Adapted with permission.<sup>107</sup> Copyright 2012, John Wiley and Sons.

### 2.7.3 Batteries/Energy Storage

Robust COFs with enhanced structural stability, low solubility, and open pore channels are suitable for the transport of ions and electrons. In addition, the COF backbone can be modified with redox-active centers for storing or liberating lithium or sodium ions, which makes them interesting materials for application in batteries or energy storage.

For this purpose, a redox-active, crystalline, mesoporous D<sub>TP</sub>-A<sub>NDI</sub>-COF was deposited on the outer surface of carbon nanotubes (CNTs) *via* the *in situ* condensation of D<sub>TP</sub>-A<sub>NDI</sub>-COF in the presence of CNT wires under solvothermal conditions.<sup>130</sup> The COF is insoluble in the electrolyte solution, giving electrodes with robust structural stability. Moreover, owing to the presence of aligned open mesoporous channels, ion transport was facilitated, with the redox-active COF walls undergoing multi-electron oxidation and reduction processes and the carbon nanotube wires contributing to enhanced electron conductivity compared to the pristine COF (Fig. 18). Furthermore, the great availability of different redox-active building blocks and the versatility of COF synthesis in combination with conducting carbons make this approach a very important step towards facilitating the synthesis of electrode materials for energy storage.



**Fig. 18.** (a) Schematic illustration of the AA-stacking of DTP-ANDI-COF with redox-active naphthalene diimide walls. (b) Chemical structure of DTP-ANDI-COF. (c) Electrochemical redox reaction of the naphthalene diimide unit. (d) Photographs of a coin-type battery. (e) Graphical representation of DTP-ANDI-COF@CNT, electron conduction, and ion transport. CNTs are depicted in grey. (f) Discharge-charge curves of DTP-ANDI-COF@CNTs upon 100 cycles at the rate of 2.4 C (red, 1<sup>st</sup> cycle; orange, 10<sup>th</sup> cycle; yellow, 20<sup>th</sup> cycle; green, 50<sup>th</sup> cycle; blue, 80<sup>th</sup> cycle; purple, 100<sup>th</sup> cycle). (g) Capacities of DTP-ANDI-COF@CNTs (red line) and CNT (dotted black line) batteries and Coulombic efficiency of DTP-ANDI-COF@CNTs for 100 cycles (black line). Adapted with permission.<sup>130</sup> Copyright 2015, Springer Nature.

Boroxine-linked 2D PPTODB COF, prepared from 4,5,9,10-tetraone-pyrene-2,7-diboronic acid, features redox active tetraone sites protruding the pore walls.<sup>131</sup> By mixing 70 wt% of the PPTODB COF with 30 wt% CNTs as a conductive additive, a binder-free organic cathode material for lithium-ion storage was obtained. Lithium-ion batteries (LIBs) with high electrochemical performance, specific capacity of 198 mAh g<sup>-1</sup>, rate ability (76%, 1000 mA g<sup>-1</sup> vs. 100 mA g<sup>-1</sup>), and stable coulombic efficiency (CE, ~99.6% at 150<sup>th</sup> cycle) were obtained, which was attributed to the high electrochemical activity (4 redox electrons) of the tetraone sites combined with an enhanced  $\pi$ - $\pi$  interaction between PPTODB and the CNTs.

COFs were reported by Vazquez-Molina *et al.* to be mechanically pressed into shaped objects, leading to anisotropic crystallographic ordering of the COF sheets with preferred orientation between the (hk0) and (00l) crystallographic planes.<sup>132</sup> Different boronic-acid-derived COFs with different functionality and symmetry (COF-1, COF-5, ZnPc-PBBA) were analyzed using this approach showing exceptional stability and similar crystallographic behavior in terms of crystallographic preferred orientation for all these structures. Room temperature conductivity of up to 0.26 mS cm<sup>-1</sup> was obtained for a pressed pellet made from LiClO<sub>4</sub>-impregnated bulk COF-5 powders. In another study, COF-1 was used as functional additive in solid polymer electrolytes for LIBs.<sup>102</sup> In that report, poly(vinylidene fluoride)

(PVDF) composites containing  $\text{LiClO}_4$  and COF-1 were prepared by a solution casting technique. Thereby, polymer electrolyte PVDF was dissolved in *N*-methyl-2-pyrrolidone, COF-1 powder was subsequently added to the polymer solution, the solution was stirred at room temperature for 1 day, and afterwards spread on a clean glass plate using a doctor blade apparatus. After solidifying and drying, the membranes were peeled off from the glass plate. The presence of boron-containing COF-1 in the electrolytes enabled a strong adsorption of the anions of the lithium salt by the boron groups in the framework, resulting in an improved Li ion transference number when using COF-containing polymer electrolytes. In this way, decreased overpotentials as well as improved rate performances were achieved for the solid-state cells with COF-containing polymer electrolytes. For example,  $\text{Li/PVDF/H-COF-1@10/LiFePO}_4$  exhibited an initial capacity of  $128 \text{ mAh g}^{-1}$  and a capacity retention of 94% after 80 cycles. Moreover, it showed discharge capacities of  $\sim 145$ , 138, 128, 122, and  $107 \text{ mAh g}^{-1}$  at 0.25 C, 0.5 C, 1 C, 2 C, and 4 C rates, respectively. The authors postulate that by using functionalized COF structures that contain electron-withdrawing groups, the Li ion transference number may be even further improved.

Yoo *et al.* utilized a hybrid material consisting of COF-1 or COF-5 on CNTs as a hierarchical porous chemical trap for lithium polysulfides ( $\text{Li}_2\text{S}_x$ ) for Li-S batteries.<sup>90</sup> A CNT-templated *in situ* COF synthesis assisted by the favorable CNT/COF  $\pi$ - $\pi$  interactions was employed, giving access to microporous-COF-on-mesoporous-CNT hybrids. DFT calculations revealed that the combination of microporous COFs as  $\text{Li}_2\text{S}_x$  traps with mesoporous CNTs as ion-conducting channels had a beneficial influence on the electrochemical performance of the Li-S-cells, attributed to the boron-mediated chemical affinity for selectively binding  $\text{Li}_2\text{S}$ . As opposed to COF-5 with its larger pore size of 2.7 nm, COF-1 with smaller micropores of 0.7 nm allowed for the exclusive penetration of  $\text{Li}_2\text{S}$ , leading to its selective adsorption. The COF-1 composite also facilitated the solid-liquid conversion of  $\text{Li}_2\text{S}$ , leading to an improvement in the electrochemical reversibility, and thus an exceptional improvement in the cell performance was observed, *i.e.* a capacity retention after 300 cycles (at a rate of 2.0 C/2.0 C) of 84% was obtained compared to 15% for a control cell without COF interlayer.

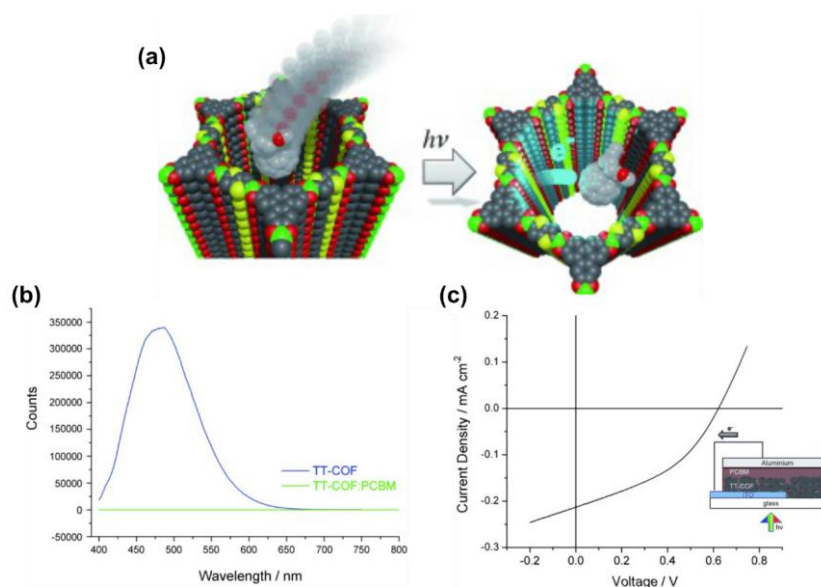
Using the *in situ* growth approach, an anode material for potassium-ion batteries (PIBs) was prepared consisting of COF-10 (Table 2) and carbon nanotubes (COF-10@CNT).<sup>133</sup> The enhanced  $\pi$ - $\pi$  stacking in the hybrid COF-10@CNT structure facilitates the access to the exposed active sites, and accordingly, ion/electron diffusion was shortened and the insertion/extraction kinetics of potassium ions were improved. High capacities of  $288 \text{ mAh g}^{-1}$  after 500 cycles at  $0.1 \text{ A g}^{-1}$  and  $161 \text{ mAh g}^{-1}$  after 4000 cycles at  $1 \text{ A g}^{-1}$  were detected.

## 2.7.4 Optoelectronics

A prominent feature of 2D COFs is the precise alignment of aromatic, photoactive, and semiconducting molecular slabs into defined molecular stacks guided by  $\pi$ - $\pi$  interactions between successive COF layers. The tight arrangement of the molecular stacks is expected to grant access to a charge-carrier path and facilitate charge migration along the stacking direction, making these materials attractive for optoelectronic applications. Furthermore, available pores in the mesoporous scale are suitable for

hosting guest molecules with matching electronic properties to create an ordered photoactive blend. To this end, boronate ester COFs have been designed and synthesized aiming at the formation of a photoactive backbone and structurally defined donor–acceptor blends as powder bulk materials,<sup>134</sup> and their deposition as oriented thin films on conductive substrates has allowed their exploration as photoactive devices (section 2.6.2).

The first COF-based photovoltaic device was reported by Bein and co-workers using TT-COF (Table 2), which combines thieno[2,3-b]thiophene diboronic acid building block as electron donor with HHTP.<sup>57</sup> The obtained COF featured high surface area of up to  $1810 \text{ m}^2 \text{ g}^{-1}$  and open pore system, which was used for the infiltration of a complementary electron acceptor [6,6]-phenyl-C<sub>61</sub>-butyric acid methyl ester (PCBM). A light-induced charge transfer from the photoactive TT-COF donor framework to the acceptor PCBM encapsulated in the pores was observed in spectroscopic measurements. Photoluminescence measurements revealed drastic quenching upon inclusion, indicating a charge transfer from the COF backbone to the included guest (Fig. 19). Thereafter, a photovoltaic device was constructed by depositing TT-COF on glass-modified ITO substrate electrode as an oriented thin film by the non-epitaxial *in situ* method (for more details, see section 2.3.2). Subsequently, PCBM was infiltrated into the open and vertically aligned COF pores by soaking and spin coating. To finalize the photovoltaic device, a thin Al layer was deposited as a top electrode. With the obtained photovoltaic COF device, charge migration and collection were observed for the first time. Under simulated AM1.5G full sun illumination, an open-circuit voltage of 622 mV, a short-circuit current density of  $0.213 \text{ mA cm}^{-2}$ , and 40% fill factor were obtained, giving a power conversion efficiency of 0.053%.

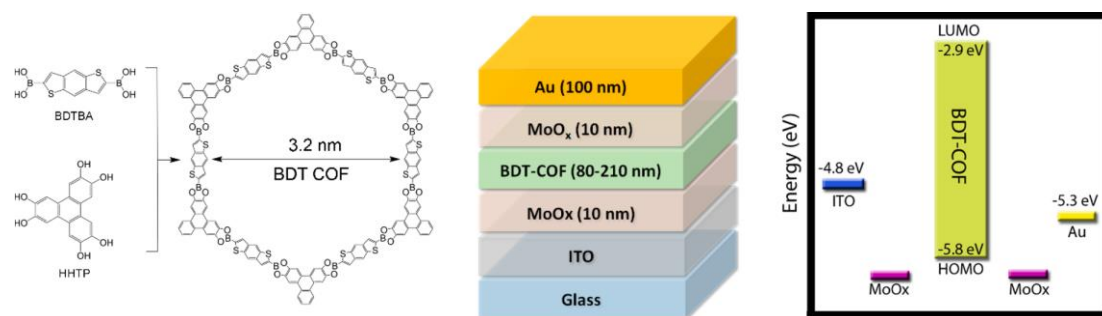


**Fig. 19.** (a) Schematic representation of the encapsulation of a PCBM molecule in the pore of TT-COF and the light-induced charge transfer from the TT-COF donor to the acceptor molecule. (b) Fluorescence emission of TT-COF (blue) upon excitation at  $\lambda = 380 \text{ nm}$  and after encapsulation of PCBM (green). (c)  $I$ – $V$  characteristics of the TT-COF-based photovoltaic cell measured under illumination with simulated solar light. Adapted with permission.<sup>57</sup> Copyright 2013, John Wiley and Sons.

In a later work, employing an approach combining both the donor and acceptor within the framework, TP-Por COF (Table 2) containing both electron-donor porphyrin and electron-acceptor HHTP was synthesized resulting in a highly defined interdigitated donor–acceptor heterojunction.<sup>54</sup> To examine the

charge migration properties of the COF, oriented thin films of the material were grown using the non-epitaxial *in situ* approach on patterned ITO substrates covered with a 10 nm layer of vacuum-deposited MoO<sub>x</sub>. To complete the device, ZnO/Al served as the top electrode. Upon irradiation with simulated solar light, an open-circuit voltage of 312 mV and a short-circuit current density of 44.6  $\mu\text{A cm}^{-2}$  were obtained.

To estimate the hole charge carrier transport in boronate ester COFs exclusively along the layer stacks, hole-only devices were constructed by Medina *et al.*<sup>61</sup> For this purpose, oriented thin films of photoactive BDT-COF were grown on glass-supported ITO with hole-selective layer of MoO<sub>x</sub> (Fig. 20). Subsequently, a top MoO<sub>x</sub> layer and gold electrode were deposited on top of the oriented film to complete the device. The directional charge transport of the oriented BDT-COF thin films was exclusively examined along the  $\pi$ -columnar arrays and electrical conductivity was examined in the COF planes. Depending on the thickness of the COF films, different hole mobilities were observed, and thinner films revealed higher average hole mobilities ( $3 \times 10^{-7} \text{ cm}^2 \text{ V}^{-1} \text{ s}^{-1}$  for a thickness of 80–100 nm) than the respective thicker (~200 nm) ones. This variation was attributed to transport barriers that appear within the BDT-COF stacks. Moreover, for the 200 nm thick sample, an increase of one order of magnitude in hole mobility was observed under illumination ( $3 \times 10^{-8} \text{ cm}^2 \text{ V}^{-1} \text{ s}^{-1}$ ) compared to the measurement in the dark ( $5 \times 10^{-9} \text{ cm}^2 \text{ V}^{-1} \text{ s}^{-1}$ ), revealing the photoactive nature of BDT-COF.



**Fig. 20.** Schematic representation of BDT-COF-based hole-only device, the COF structure, and the corresponding energy diagram. Reprinted with permission.<sup>61</sup> Copyright (2017) American Chemical Society.

## 2.7.5 Other Applications

In addition to the applications described above, examples for the use of boronic-acid-derived COFs have been reported for a variety of other applications as well. Recently, boroxine-linked COF-1 was shown to facilitate nitrogen accessibility in nitrogen reduction reaction (NRR) to ammonia through electrochemical excitation.<sup>135</sup> Simulations showed outstanding electronic structure of COF-1 for N<sub>2</sub> absorption and a reduced energy barrier of the rate-determining step, N<sub>2</sub> dissociation, over the boron-sites of the COF. Therefore, when suitable potential was applied, boron atoms easily bonded with the nitrogen species, causing distortions in the lattice planes of the COF, which led to enhanced nitrogen adsorption towards the framework. The whole NRR reaction was facilitated due to the localized high nitrogen concentration that promotes the probability of collisions of nitrogen molecules with the boron sites. The conclusions from this study were verified by proof-of-concept experiments on COF-1 on nitrogen-doped carbon nanosheet support. XRD measurements indicated that the COF transformed from crystalline to

amorphous, while *in situ* Raman experiments verified the formation of the B–N bond during electrochemical excitation. The ability to facilitate the NRR due to the transformations in the COF structure was demonstrated by linear sweep voltammetry studies, showing that COF-1 on nitrogen-doped carbon nanosheet produced ammonia with Faradaic efficiency of 45.43%.

Spray-coated 2D COF thin films (section 2.6.2) were incorporated as the active layer in acoustic sensors by Evans *et al.*<sup>124</sup> To this end, COF-5 ink was spray-coated onto Ti-coated QCM acoustic resonators, and the resulting 2D COF QCM-based volatile amine sensor was employed for the detection of volatile amines in meat and seafood, such as trimethylamine (TMA). Here, remarkable performance was observed, which was attributed to the porosity and Lewis acidity provided by the boron of the 2D COF: TMA could be detected at concentrations as low as 10 ppb, placing these 2D COF-based sensors among the most sensitive sensors for food spoilage.

### 3. Summary and Outlook

Boronic-acid-containing building blocks have paved the way for the construction of robust, thermally stable hierarchical materials with key features such as long-range order and well-defined cavities, the so-called covalent organic frameworks. The reversible nature of the boronic acid condensation reaction, allowing for “proof-reading” processes during the synthesis, has thus resulted in the synthesis of complex structures not attainable through other methods. Thereafter, the field of COFs has expanded to feature a much larger diversity of linkages.

Boronic-acid-bearing building blocks have played a pivotal role in giving the first insights into the formation of COFs, their crystallization, growth as bulk and films, and their utilization. Although the COF field is currently dominated by structures based on imine linkages, boronic-acid-derived COFs offer exceptional opportunities of atomically precise design owing to their excellent crystallinity. They are particularly suitable for studying the mechanism of COF formation owing to their high reactivity under mild conditions, sometimes at room temperature, without the need of a catalyst, such as acid or base, which facilitates the interpretation of the COF formation process. In addition, boronate ester and boroxine moieties are in-plane linkages, which position the typically planar aromatic COF building blocks at an optimal geometry for  $\pi$ – $\pi$  stacking, forming closely packed aggregates in a solid matrix. Additionally, given that these linkages are not conjugation junctions, they enable the creation of ordered interdigitated molecular aggregates of different properties, such as electron donor–acceptor, where the boronate ester acts as an integral junction. Also, highly sensitive sensors can be constructed from boronate ester COF materials based on the strong affinity of boron to electron-donating elements, such as nitrogen-containing compounds. In addition, recent reports on catalysis show that these materials can be used as pre-catalysts to give access to highly active materials.

In addition to holding promise for several applications, boronic-acid-derived COFs allow not only the study of the formation of COF materials, but interactions within the COFs and other relevant fundamental behavior. Therefore, we believe that exciting examples on the synthesis and application of these materials will continue appearing and the boronic-acid-derived COFs will hold their place within the expanding field of COFs.

## Conflicts of interest

There are no conflicts to declare.

## Acknowledgements

The authors are grateful for financial support from the Excellence Clusters “Nanosystems Initiative Munich (NIM)”, and from the Free State of Bavaria through the Research Network “Solar Technologies go Hybrid”. This work received funding from the European Union’s H2020-MSCA-IF-2018 program under the grant agreement CO2COFs number 844313, and the COFforH2 project (UTA-EXPL/NPN/0055/2019) through the Portuguese Foundation for Science and Technology funds under UT Austin Portugal.

## References

- 1 A. P. Côté, A. I. Benin, N. W. Ockwig, M. O’Keeffe, A. J. Matzger and O. M. Yaghi, *Science*, 2005, **310**, 1166–1170.
- 2 D. Hall, in *Boronic Acids: Preparation and Applications in Organic Synthesis and Medicine*, 2006, pp. 1–99.
- 3 D. G. Hall, *Chem. Soc. Rev.*, 2019, **48**, 3475–3496.
- 4 A. Suzuki, *Angew. Chem. Int. Ed.*, 2011, **50**, 6722–6737.
- 5 R. Nishiyabu, Y. Kubo, T. D. James and J. S. Fossey, *Chem. Commun.*, 2011, **47**, 1106–1123.
- 6 X. Wu, Z. Li, X.-X. Chen, J. S. Fossey, T. D. James and Y.-B. Jiang, *Chem. Soc. Rev.*, 2013, **42**, 8032–8048.
- 7 G. Zhang, O. Presly, F. White, I. M. Oppel and M. Mastalerz, *Angew. Chem. Int. Ed.*, 2014, **53**, 1516–1520.
- 8 N. Nishimura and K. Kobayashi, *J. Org. Chem.*, 2010, **75**, 6079–6085.
- 9 E. Sheepwash, N. Luisier, M. R. Krause, S. Noé, S. Kubik and K. Severin, *Chem. Commun.*, 2012, **48**, 7808–7810.
- 10 M. K. Smith and B. H. Northrop, *Chem. Mater.*, 2014, **26**, 3781–3795.
- 11 J.-H. Fournier, T. Maris, J. D. Wuest, W. Guo and E. Galoppini, *J. Am. Chem. Soc.*, 2003, **125**, 1002–1006.
- 12 H. M. El-Kaderi, J. R. Hunt, J. L. Mendoza-Cortés, A. P. Côté, R. E. Taylor, M. O’Keeffe and O. M. Yaghi, *Science*, 2007, **316**, 268–272.
- 13 N. Huang, X. Ding, J. Kim, H. Ihee and D. Jiang, *Angew. Chem. Int. Ed.*, 2015, **54**, 8704–8707.
- 14 J. Zhang, L. Wang, N. Li, J. Liu, W. Zhang, Z. Zhang, N. Zhou and X. Zhu, *CrystEngComm*, 2014, **16**, 6547–6551.
- 15 D. N. Coventry, A. S. Batsanov, A. E. Goeta, J. A. K. Howard, T. B. Marder and R. N. Perutz, *Chem. Commun.*, 2005, 2172–2174.
- 16 K. M. Waltz and J. F. Hartwig, *Science*, 1997, **277**, 211.
- 17 S. Shimada, A. S. Batsanov, J. A. K. Howard and T. B. Marder, *Angew. Chem. Int. Ed.*, 2001, **40**, 2168–2171.
- 18 H. Chen, S. Schlecht, T. C. Semple and J. F. Hartwig, *Science*, 2000, **287**, 1995.
- 19 T. Ishiyama, J. Takagi, K. Ishida, N. Miyaura, N. R. Anastasi and J. F. Hartwig, *J. Am. Chem. Soc.*, 2002, **124**, 390–391.
- 20 J.-Y. Cho, C. N. Iverson and M. R. Smith, *J. Am. Chem. Soc.*, 2000, **122**, 12868–12869.
- 21 S. Wan, J. Guo, J. Kim, H. Ihee and D. Jiang, *Angew. Chem. Int. Ed.*, 2008, **47**, 8826–8830.
- 22 A. G. Crawford, Z. Liu, I. A. I. Mkhalid, M.-H. Thibault, N. Schwarz, G. Alcaraz, A. Steffen, J. C. Collings, A. S. Batsanov, J. A. K. Howard and T. B. Marder, *Chemistry*, 2012, **18**, 5022–5035.
- 23 A. R. Goldberg and B. H. Northrop, *J. Org. Chem.*, 2016, **81**, 969–980.
- 24 O. R. Cromwell, J. Chung and Z. Guan, *J. Am. Chem. Soc.*, 2015, **137**, 6492–6495.
- 25 K. L. Bhat, G. D. Markham, J. D. Larkin and C. W. Bock, *J. Phys. Chem. A*, 2011, **115**, 7785–7793.
- 26 J. P. M. António, R. Russo, C. P. Carvalho, Cal, Pedro M. S. D. and P. M. P. Gois, *Chem. Soc. Rev.*, 2019, **48**, 3513–3536.
- 27 B. Marco-Dufort and M.W. Tibbitt, *Mater. Today Chem.*, 2019, **12**, 16–33.

- 28 X. Wu, Z. Li, X.-X. Chen, J. S. Fossey, T. D. James and Y.-B. Jiang, *Chem. Soc. Rev.*, 2013, **42**, 8032–8048.
- 29 X. Feng, X. Ding and D. Jiang, *Chem. Soc. Rev.*, 2012, **41**, 6010–6022.
- 30 S. Kandambeth, K. Dey and R. Banerjee, *J. Am. Chem. Soc.*, 2019, **141**, 1807–1822.
- 31 M. S. Lohse and T. Bein, *Adv. Funct. Mater.*, 2018, **28**, 1705553.
- 32 N. L. Campbell, R. Clowes, L. K. Ritchie and A. I. Cooper, *Chem. Mater.*, 2009, **21**, 204–206.
- 33 S.-T. Yang, J. Kim, H.-Y. Cho, S. Kim and W.-S. Ahn, *RSC Adv.*, 2012, **2**, 10179–10181.
- 34 B. J. Smith and W. R. Dichtel, *J. Am. Chem. Soc.*, 2014, **136**, 8783–8789.
- 35 B. J. Smith, N. Hwang, A. D. Chavez, J. L. Novotney and W. R. Dichtel, *Chem. Commun.*, 2015, **51**, 7532–7535.
- 36 H. Li, A. D. Chavez, H. Li, H. Li, W. R. Dichtel and J.-L. Bredas, *J. Am. Chem. Soc.*, 2017, **139**, 16310–16318.
- 37 H. Li, A. M. Evans, I. Castano, M. J. Strauss, W. R. Dichtel and J.-L. Bredas, *J. Am. Chem. Soc.*, 2020, **142**, 1367–1374.
- 38 M. Niederberger and H. Cölfen, *Phys. Chem. Chem. Phys.*, 2006, **8**, 3271–3287.
- 39 D. D. Medina and Y. Mastai, *Cryst. Growth Des.*, 2008, **8**, 3646–3651.
- 40 H. Cölfen, *Crystals*, 2020, **10**.
- 41 A. M. Evans, L. R. Parent, N. C. Flanders, R. P. Bisbey, E. Vitaku, M. S. Kirschner, R. D. Schaller, L. X. Chen, N. C. Gianneschi and W. R. Dichtel, *Science*, 2018, **361**, 52–57.
- 42 S. Wan, J. Guo, J. Kim, H. Ihee and D. Jiang, *Angew. Chem. Int. Ed.*, 2009, **48**, 5439–5442.
- 43 L. A. Baldwin, J. W. Crowe, M. D. Shannon, C. P. Jaroniec and P. L. McGrier, *Chem. Mater.*, 2015, **27**, 6169–6172.
- 44 L. A. Baldwin, J. W. Crowe, D. A. Pyles and P. L. McGrier, *J. Am. Chem. Soc.*, 2016, **138**, 15134–15137.
- 45 J. W. Crowe, L. A. Baldwin and P. L. McGrier, *J. Am. Chem. Soc.*, 2016, **138**, 10120–10123.
- 46 X. Feng, Y. Dong and D. Jiang, *CrystEngComm*, 2013, **15**, 1508–1511.
- 47 H. Yang, Y. Du, S. Wan, G. D. Trahan, Y. Jin and W. Zhang, *Chem. Sci.*, 2015, **6**, 4049–4053.
- 48 S. Dalapati, E. Jin, M. Addicoat, T. Heine and D. Jiang, *J. Am. Chem. Soc.*, 2016, **138**, 5797–5800.
- 49 A. P. Côté, H. M. El-Kaderi, H. Furukawa, J. R. Hunt and O. M. Yaghi, *J. Am. Chem. Soc.*, 2007, **129**, 12914–12915.
- 50 L. M. Salonen, D. D. Medina, E. Carbó-Argibay, M. G. Goesten, L. Mafra, N. Guldreis, J. M. Rotter, D. G. Stroppa and C. Rodríguez-Abreu, *Chem. Commun.*, 2016, **52**, 7986–7989.
- 51 E. L. Spitler, B. T. Koo, J. L. Novotney, J. W. Colson, F. J. Uribe-Romo, G. D. Gutierrez, P. Clancy and W. R. Dichtel, *J. Am. Chem. Soc.*, 2011, **133**, 19416–19421.
- 52 S. Rager, M. Dogru, V. Werner, A. Gavryushin, M. Götz, H. Engelke, D. D. Medina, P. Knochel and T. Bein, *CrystEngComm*, 2017, **19**, 4886–4891.
- 53 R. P. P., P. K. Mondal and D. Chopra, *J. Chem. Sci.*, 2018, **130**, 51.
- 54 M. Calik, F. Auras, L. M. Salonen, K. Bader, I. Grill, M. Handloser, D. D. Medina, M. Dogru, F. Löbermann, D. Trauner, A. Hartschuh and T. Bein, *J. Am. Chem. Soc.*, 2014, **136**, 17802–17807.
- 55 X. Feng, L. Chen, Y. Honsho, O. Saengsawang, L. Liu, L. Wang, A. Saeki, S. Irle, S. Seki, Y. Dong and D. Jiang, *Adv. Mater.*, 2012, **24**, 3026–3031.
- 56 G. H. V. Bertrand, V. K. Michaelis, T.-C. Ong, R. G. Griffin and M. Dincă, *Proc. Natl. Acad. Sci. U. S. A.*, 2013, **110**, 4923–4928.
- 57 M. Dogru, M. Handloser, F. Auras, T. Kunz, D. Medina, A. Hartschuh, P. Knochel and T. Bein, *Angew. Chem. Int. Ed.*, 2013, **52**, 2920–2924.
- 58 Y. Chen, H. Cui, J. Zhang, K. Zhao, D. Ding, J. Guo, L. Li, Z. Tian and Z. Tang, *RSC Adv.*, 2015, **5**, 92573–92576.
- 59 D. D. Medina, V. Werner, F. Auras, R. Tautz, M. Dogru, J. Schuster, S. Linke, M. Döblinger, J. Feldmann, P. Knochel and T. Bein, *ACS Nano*, 2014, **8**, 4042–4052.
- 60 D. D. Medina, J. M. Rotter, Y. Hu, M. Dogru, V. Werner, F. Auras, J. T. Markiewicz, P. Knochel and T. Bein, *J. Am. Chem. Soc.*, 2015, **137**, 1016–1019.
- 61 D. D. Medina, M. L. Petrus, A. N. Jumabekov, J. T. Margraf, S. Weinberger, J. M. Rotter, T. Clark and T. Bein, *ACS Nano*, 2017, **11**, 2706–2713.
- 62 M. S. Lohse, J. M. Rotter, J. T. Margraf, V. Werner, M. Becker, S. Herbert, P. Knochel, T. Clark, T. Bein and D. D. Medina, *CrystEngComm*, 2016, **18**, 4295–4302.
- 63 S. Duhović and M. Dincă, *Chem. Mater.*, 2015, **27**, 5487–5490.
- 64 S. Rager, A. C. Jakowetz, B. Gole, F. Beuerle, D. D. Medina and T. Bein, *Chem Mater*, 2019, **31**, 2707–2712.
- 65 R. W. Tilford, W. R. Gemmill, H.-C. zur Loye and J. J. Lavigne, *Chem. Mater.*, 2006, **18**, 5296–5301.

- 66 M. Dogru, A. Sonnauer, A. Gavryushin, P. Knochel and T. Bein, *Chem. Commun.*, 2011, **47**, 1707–1709.
- 67 X. Ding, L. Chen, Y. Honsho, X. Feng, O. Saengsawang, J. Guo, A. Saeki, S. Seki, S. Irle, S. Nagase, V. Parasuk and D. Jiang, *J. Am. Chem. Soc.*, 2011, **133**, 14510–14513.
- 68 J.-T. Yu, Z. Chen, J. Sun, Z.-T. Huang and Q.-Y. Zheng, *J. Mater. Chem.*, 2012, **22**, 5369–5373.
- 69 R. Liang, Y. Hu and G. Li, *J. Chromatogr., A*, 2020, 460867.
- 70 J. Zhen, S. Ding, W. Wang, J. Liu, J. Sun, Z. Huang and Q. Zheng, *Chin. J. Chem.*, 2016, **34**, 783–787.
- 71 X. Feng, L. Liu, Y. Honsho, A. Saeki, S. Seki, S. Irle, Y. Dong, A. Nagai and D. Jiang, *Angew. Chem. Int. Ed.*, 2012, **51**, 2618–2622.
- 72 S. Ghosh and J. K. Singh, *Int. J. Hydrog. Energy*, 2019, **44**, 1782–1796.
- 73 A. B. Sorokin, *Chem. Rev.*, 2013, **113**, 8152–8191.
- 74 E. L. Spittler, J. W. Colson, F. J. Uribe-Romo, A. R. Woll, M. R. Giovino, A. Saldivar and W. R. Dichtel, *Angew. Chem. Int. Ed.*, 2012, **51**, 2623–2627.
- 75 E. L. Spittler and W. R. Dichtel, *Nat. Chem.*, 2010, **2**, 672–677.
- 76 X. Ding, X. Feng, A. Saeki, S. Seki, A. Nagai and D. Jiang, *Chem. Commun.*, 2012, **48**, 8952–8954.
- 77 S. Wan, F. Gándara, A. Asano, H. Furukawa, A. Saeki, S. K. Dey, L. Liao, M. W. Ambrogio, Y. Y. Botros, X. Duan, S. Seki, J. F. Stoddart and O. M. Yaghi, *Chem. Mater.*, 2011, **23**, 4094–4097.
- 78 N. Huang, L. Zhai, D. E. Coupry, M. A. Addicoat, K. Okushita, K. Nishimura, T. Heine and D. Jiang, *Nat. Commun.*, 2016, **7**, 12325.
- 79 S. Jin, K. Furukawa, M. Addicoat, L. Chen, S. Takahashi, S. Irle, T. Nakamura and D. Jiang, *Chem. Sci.*, 2013, **4**, 4505–4511.
- 80 S. Jin, M. Supur, M. Addicoat, K. Furukawa, L. Chen, T. Nakamura, S. Fukuzumi, S. Irle and D. Jiang, *J. Am. Chem. Soc.*, 2015, **137**, 7817–7827.
- 81 W. Budiawan, K.-W. Lai, P. Karuppuswamy, T. S. Jadhav, Y.-A. Lu, K.-C. Ho, P.-C. Wang, C.-C. Chang and C.-W. Chu, *ACS Appl. Mater. Interfaces*, 2020, **12**.
- 82 M. Martínez-Abadía, C. T. Stoppiello, K. Strutynski, B. Lerma-Berlanga, C. Martí-Gastaldo, A. Saeki, M. Melle-Franco, A. N. Khlobystov and A. Mateo-Alonso, *J. Am. Chem. Soc.*, 2019, **141**, 14403–14410.
- 83 M. A. A. Musa, C.-Y. Yin and R. M. Savory, *Mater. Chem. Phys.*, 2010, **123**, 5–8.
- 84 J. F. Dienstmaier, A. M. Gigler, A. J. Goetz, P. Knochel, T. Bein, A. Lyapin, S. Reichlmaier, W. M. Heckl and M. Lackinger, *ACS Nano*, 2011, **5**, 9737–9745.
- 85 J. F. Dienstmaier, D. D. Medina, M. Dogru, P. Knochel, T. Bein, W. M. Heckl and M. Lackinger, *ACS Nano*, 2012, **6**, 7234–7242.
- 86 H. Oh, S. B. Kalidindi, Y. Um, S. Bureekaew, R. Schmid, R. A. Fischer and M. Hirscher, *Angew. Chem. Int. Ed.*, 2013, **52**, 13219–13222.
- 87 S. B. Kalidindi, C. Wiktor, A. Ramakrishnan, J. Weßing, A. Schneemann, G. van Tendeloo and R. A. Fischer, *Chem. Commun.*, 2013, **49**, 463–465.
- 88 D. Cui, J. M. MacLeod, M. Ebrahimi and F. Rosei, *CrystEngComm*, 2017, **19**, 4927–4932.
- 89 J. Plas, O. Ivasenko, N. Martsinovich, M. Lackinger and S. de Feyter, *Chem. Commun.*, 2016, **52**, 68–71.
- 90 J. Yoo, S.-J. Cho, G. Y. Jung, S. H. Kim, K.-H. Choi, J.-H. Kim, C. K. Lee, S. K. Kwak and S.-Y. Lee, *Nano Lett.*, 2016, **16**, 3292–3300.
- 91 Y. Chen and Z. Chen, *Talanta*, 2017, **165**, 188–193.
- 92 Y. Du, D. Calabro, B. Wooler, Q. Li, S. Cundy, P. Kamakoti, D. Colmyer, K. Mao and P. Ravikovitch, *J. Phys. Chem.*, 2014, **118**, 399–407.
- 93 Y. Du, K. Mao, P. Kamakoti, B. Wooler, S. Cundy, Q. Li, P. Ravikovitch and D. Calabro, *J. Mater. Chem. A*, 2013, **1**, 13171–13178.
- 94 Y. Du, D. Calabro, B. Wooler, P. Kortunov, Q. Li, S. Cundy and K. Mao, *Chem. Mater.*, 2015, **27**, 1445–1447.
- 95 D. Cui, J. M. MacLeod, M. Ebrahimi, D. F. Perepichka and F. Rosei, *Chem. Commun.*, 2015, **51**, 16510–16513.
- 96 G. Li, K. Zhang and T. Tsuru, *ACS Appl. Mater. Interfaces*, 2017, **9**, 8433–8436.
- 97 S. Spitzer, A. Rastgoo-Lahrood, K. Macknapp, V. Ritter, S. Sotier, W. M. Heckl and M. Lackinger, *Chem. Commun.*, 2017, **53**, 5147–5150.
- 98 T. Pham, K. A. Forrest, M. Mostrom, J. R. Hunt, H. Furukawa, J. Eckert and B. Space, *Phys. Chem. Chem. Phys.*, 2017, **19**, 13075–13082.
- 99 Zhao Hui et al, *Mater. Res. Express*, 2020.
- 100 J. Sun, A. Iakunkov, I. A. Baburin, B. Joseph, V. Palermo and A. V. Talyzin, *Angew. Chem. Int. Ed.*, 2020, **59**, 1087–1092.

- 101X. Zhang, H. Li, J. Wang, D. Peng, J. Liu and Y. Zhang, *J. Membr. Sci.*, 2019, **581**, 321–330.
- 102D. Dong, H. Zhang, B. Zhou, Y. Sun, H. Zhang, M. Cao, J. Li, H. Zhou, H. Qian, Z. Lin and H. Chen, *Chem. Commun.*, 2019, **55**, 1458–1461.
- 103J. Sun, A. Klechikov, C. Moise, M. Prodana, M. Enachescu and A. V. Talyzin, *Angew. Chem. Int. Ed.*, 2018, **57**, 1034–1038.
- 104C. Liu, W. Zhang, Q. Zeng and S. Lei, *Chemistry*, 2016, **22**, 6768–6773.
- 105S. S. Han, H. Furukawa, O. M. Yaghi and W. A. Goddard, *J. Am. Chem. Soc.*, 2008, **130**, 11580–11581.
- 106D. N. Bunck and W. R. Dichtel, *Angew. Chem. Int. Ed.*, 2012, **51**, 1885–1889.
- 107S. B. Kalidindi, H. Oh, M. Hirscher, D. Esken, C. Wiktor, S. Turner, G. van Tendeloo and R. A. Fischer, *Chemistry*, 2012, **18**, 10848–10856.
- 108S. D. Brucks, D. N. Bunck and W. R. Dichtel, *Polymer*, 2014, **55**, 330–334.
- 109H. Ma, H. Ren, S. Meng, Z. Yan, H. Zhao, F. Sun and G. Zhu, *Chem. Commun.*, 2013, **49**, 9773–9775.
- 110Y. Zeng, R. Zou, Z. Luo, H. Zhang, X. Yao, X. Ma, R. Zou and Y. Zhao, *J. Am. Chem. Soc.*, 2015, **137**, 1020–1023.
- 111X. Chen, M. Addicoat, E. Jin, H. Xu, T. Hayashi, F. Xu, N. Huang, S. Irle and D. Jiang, *Sci. Rep.*, 2015, **5**, 14650.
- 112H. Li, Q. Pan, Y. Ma, X. Guan, M. Xue, Q. Fang, Y. Yan, V. Valtchev and S. Qiu, *J. Am. Chem. Soc.*, 2016, **138**, 14783–14788.
- 113J.-Y. Yue, Y.-P. Mo, S.-Y. Li, W.-L. Dong, T. Chen and D. Wang, *Chem. Sci.*, 2017, **8**, 2169–2174.
- 114C. Gropp, T. Ma, N. Hanikel and O. M. Yaghi, *Science*, 2020, **370**.
- 115Y. Yusran, X. Guan, H. Li, Q. Fang and S. Qiu, *Natl. Sci. Rev.*, 2019, **7**, 170–190.
- 116J. L. Segura, S. Royuela and M. Mar Ramos, *Chem. Soc. Rev.*, 2019, **48**, 3903–3945.
- 117A. Nagai, Z. Guo, X. Feng, S. Jin, X. Chen, X. Ding and D. Jiang, *Nat. Commun.*, 2011, **2**, 536.
- 118L. Chen, K. Furukawa, J. Gao, A. Nagai, T. Nakamura, Y. Dong and D. Jiang, *J. Am. Chem. Soc.*, 2014, **136**, 9806–9809.
- 119D. N. Bunck and W. R. Dichtel, *Chem. Commun.*, 2013, **49**, 2457–2459.
- 120L. A. Baldwin, J. W. Crowe, D. A. Pyles and P. L. McGrier, *J. Am. Chem. Soc.*, 2016, **138**, 15134–15137.
- 121B. J. Smith, L. R. Parent, A. C. Overholts, P. A. Beaucage, R. P. Bisbey, A. D. Chavez, N. Hwang, C. Park, A. M. Evans, N. C. Gianneschi and W. R. Dichtel, *ACS Cent. Sci.*, 2017, **3**, 58–65.
- 122A. M. Evans, I. Castano, A. Brumberg, L. R. Parent, A. R. Corcos, R. L. Li, N. C. Flanders, D. J. Gosztola, N. C. Gianneschi, R. D. Schaller and W. R. Dichtel, *J. Am. Chem. Soc.*, 2019, **141**, 19728–19735.
- 123B. J. Smith, L. R. Parent, A. C. Overholts, P. A. Beaucage, R. P. Bisbey, A. D. Chavez, N. Hwang, C. Park, A. M. Evans, N. C. Gianneschi and W. R. Dichtel, *ACS Cent. Sci.*, 2017, **3**, 58–65.
- 124A. M. Evans, N. P. Bradshaw, B. Litchfield, M. J. Strauss, B. Seckman, M. R. Ryder, I. Castano, C. Gilmore, N. C. Gianneschi, C. R. Mulzer, M. C. Hersam and W. R. Dichtel, *Adv. Mater.*, 2020, **32**, 2004205.
- 125J. W. Colson, A. R. Woll, A. Mukherjee, M. P. Levendorf, E. L. Spitler, V. B. Shields, M. G. Spencer, J. Park and W. R. Dichtel, *Science*, 2011, **332**, 228–231.
- 126R. P. Bisbey, C. R. DeBlase, B. J. Smith and W. R. Dichtel, *J. Am. Chem. Soc.*, 2016, **138**, 11433–11436.
- 127J. M. Rotter, S. Weinberger, J. Kampmann, T. Sick, M. Shalom, T. Bein and D. D. Medina, *Chem. Mater.*, 2019, **31**, 10008–10016.
- 128J. Cai, Y. Xing and X. Zhao, *RSC Adv.*, 2012, **2**, 8579–8586.
- 129Tao Bao, Pingxiu Tang, Deying Kong, Zhenkun Mao and Zilin Chen, *J. Chromatogr., A*, 2016, **1445**, 140–148.
- 130F. Xu, S. Jin, H. Zhong, D. Wu, X. Yang, X. Chen, H. Wei, R. Fu and D. Jiang, *Sci. Rep.*, 2015, **5**, 8225.
- 131C.-J. Yao, Z. Wu, J. Xie, F. Yu, W. Guo, Z. J. Xu, D.-S. Li, S. Zhang and Q. Zhang, *ChemSusChem*, 2020, **13**, 2457.
- 132D. A. Vazquez-Molina, G. S. Mohammad-Pour, C. Lee, M. W. Logan, X. Duan, J. K. Harper and F. J. Uribe-Romo, *J. Am. Chem. Soc.*, 2016, **138**, 9767–9770.
- 133X. Chen, H. Zhang, C. Ci, W. Sun and Y. Wang, *ACS Nano*, 2019, **13**, 3600–3607.
- 134N. Keller and T. Bein, *Chem. Soc. Rev.*, 2021, **50**, 1813–1845.
- 135S. Liu, M. Wang, T. Qian, H. Ji, J. Liu and C. Yan, *Nat. Commun.*, 2019, **10**, 3898.